
Model Selection for Bayesian Autoencoders

Ba-Hien Tran
EURECOM
(France)

Simone Rossi
EURECOM
(France)

Dimitrios Miliotis
EURECOM
(France)

Pietro Michiardi
EURECOM
(France)

Edwin V. Bonilla
CSIRO's Data61 and
The University of Sydney
(Australia)

Maurizio Filippone
EURECOM
(France)

Abstract

We develop a novel method for carrying out model selection for Bayesian autoencoders (BAEs) by means of prior hyper-parameter optimization. Inspired by the common practice of type-II maximum likelihood optimization and its equivalence to Kullback-Leibler divergence minimization, we propose to optimize the distributional sliced-Wasserstein distance (DSWD) between the output of the autoencoder and the empirical data distribution. The advantages of this formulation are that we can estimate the DSWD based on samples and handle high-dimensional problems. We carry out posterior estimation of the BAE parameters via stochastic gradient Hamiltonian Monte Carlo and turn our BAE into a generative model by fitting a flexible Dirichlet mixture model in the latent space. Consequently, we obtain a powerful alternative to variational autoencoders, which are the preferred choice in modern applications of autoencoders for representation learning with uncertainty. We evaluate our approach qualitatively and quantitatively using a vast experimental campaign on a number of unsupervised learning tasks and show that, in small-data regimes where priors matter, our approach provides state-of-the-art results, outperforming multiple competitive baselines.

1 Introduction

The problem of learning useful representations of data that facilitate the solution of downstream tasks such as clustering, generative modeling and classification, is at the crux of the success of many machine learning applications [see, e.g., 5, and references therein]. From a plethora of potential solutions to this problem, unsupervised approaches based on autoencoders [13] are particularly appealing as, by definition, they do not require label information and have proved effective in tasks such as dimensionality reduction and information retrieval [27].

Autoencoders are neural network models composed of two parts, usually referred to as the encoder and the decoder. The encoder maps each input \mathbf{x}_i to a set of lower-dimensional latent variables \mathbf{z}_i . The decoder maps the latent variables \mathbf{z}_i back to the observations \mathbf{x}_i . The bottleneck introduced by the low-dimensional latent space is what characterizes the compression and representation learning capabilities of autoencoders. It is not surprising that these models have connections with principal component analysis [3], factor analysis and density networks [41], and latent variable models [35].

In applications where quantification of uncertainty is a primary requirement or where data is scarce, it is important to carry out a Bayesian treatment of these models by specifying a prior distribution over their parameters, i.e., the weights of the encoder/decoder. However, estimating the posterior distribution over the parameters of these models, which we refer to as Bayesian autoencoders (BAEs),

is generally intractable and requires approximations. Furthermore, the need to specify priors for a large number of parameters, coupled with the fact that autoencoders are not generative models, has motivated the development of Variational Autoencoders (VAEs) as an alternative that can overcome these limitations [32]. Indeed, VAEs have found tremendous success and have become one of the preferred methods in modern machine-learning applications [see, e.g., 33, and references therein].

To recap, three potential limitations of BAEs hinder their widespread applicability in order to achieve a similar or superior adoption to their variational counterpart: (i) lack of generative modeling capabilities; (ii) intractability of inference and (iii) difficulty of setting sensible priors over their parameters. In this work we revisit BAEs and deal with these limitations in a principled way. In particular, we address the first limitation in (i) by employing density estimation in the latent space. Furthermore, we deal with the second limitation in (ii) by exploiting recent advances in Markov chain Monte Carlo (MCMC) and, in particular, stochastic gradient Hamiltonian Monte Carlo (SGHMC) [11]. Finally, we believe that the third limitation (iii), which we refer to as the difficulty of carrying out *model selection*, requires a more detailed treatment because choosing sensible priors for Bayesian neural networks is an extremely difficult problem, and this is the main focus of this work.

Contributions. Specifically, in this paper we provide a novel, practical, and elegant way of performing model selection for BAEs, which allows us to revisit these models for applications where VAEs are currently the primary choice. We start by considering the common practice of estimating prior (hyper-)parameters via type-II maximum likelihood, which is equivalent to minimizing the Kullback-Leibler divergence (KL) between the distribution induced by the BAE and the data generating distribution. Because of the intractability of this objective and the difficulty to estimate it through samples, we resort to an alternative formulation where we replace the KL with the distributional sliced-Wasserstein distance (DSWD) between these two distributions. The advantages of this formulation are that we can estimate the DSWD based on samples and, thanks to the slicing, we can handle large dimensional problems. Once BAE hyper-parameters are optimized, we estimate the posterior distribution over the BAE parameters via SGHMC [11], which is a powerful sampler that operates on mini-batches and has proven effective for Bayesian deep/convolutional networks [29, 60, 68]. Furthermore, we turn our BAE into a generative model by fitting a flexible mixture model in the latent space, namely the Dirichlet Process Mixture Model (DPMM). We evaluate our approach qualitatively and quantitatively using a vast experimental campaign on a number of unsupervised learning tasks, with particular emphasis on the challenging task of generative modeling when the number of observations is small.

1.1 Related work

VAEs provide a theoretically-grounded and popular framework for representation learning and deep generative modeling. However, training VAEs poses considerable practical and theoretical challenges yet to be solved. In practice, the learned aggregated posterior distribution of the encoder rarely matches the latent prior, and this hurts the quality of generated samples. Several methods have been proposed to deal with this problem by using a more expressive form of priors on the latent space [4, 12, 48, 59]. Similar to our work, there is a line of research that employs a form of ex-post density estimation on the learned latent space [8, 14, 19]. Wasserstein Autoencoders (WAEs) [58] impose a new form of regularization on latent space by reformulating the objective function as an optimal transport (OT) problem. There have been previous attempts to apply the Bayesian approach to VAEs. For example, [16] treats the parameters of VAE’s encoder and decoder in a Bayesian manner to deal with out-of-distribution samples. Most of these works focus on imposing prior or regularization on the latent or weight space of autoencoders. In this work, we take a different route, as we aim to impose prior knowledge directly on the output space. Indeed, our work is motivated by recent attempts to rethink prior specification for Bayesian neural networks (BNNs). It is extremely difficult to choose a sensible prior on the parameters of BNNs [see, e.g., 46, and references therein] because their effect on the distribution of the induced functions is difficult to characterize. Thus, recent attempts in the literature have turned their attention towards defining priors in the space of functions [22, 47, 57, 65]. Closest to our work is that of [60], which matches the functional prior induced by BNNs to Gaussian Process (GP) priors by means of the Kantorovich-Rubinstein dual form of the Wasserstein distance. Different from this line of works, we consider a general framework to impose a functional prior for BNNs in an unsupervised learning setting.

2 Preliminaries on Bayesian Autoencoders

An autoencoder (AE) is a neural network parameterized by a set of parameters \mathbf{w} , which transforms an unlabelled dataset, $\mathbf{x} \stackrel{\text{def}}{=} \{\mathbf{x}_n\}_{n=1}^N$, into a set of reconstructions $\hat{\mathbf{x}} \stackrel{\text{def}}{=} \{\hat{\mathbf{x}}_n\}_{n=1}^N$, with $\mathbf{x}_n, \hat{\mathbf{x}}_n \in \mathbb{R}^D$. An AE is composed of two components: (1) an encoder f_{enc} which maps an input sample \mathbf{x}_n to a latent code $\mathbf{z}_n \in \mathbb{R}^K$, $K \ll D$; and (2) a decoder f_{dec} which maps the latent code to a reconstructed datapoint $\hat{\mathbf{x}}_n$. In short, $\hat{\mathbf{x}} = f(\mathbf{x}; \mathbf{w}) = (f_{\text{dec}} \circ f_{\text{enc}})(\mathbf{x})$, where we denote $\mathbf{w} := \{\mathbf{w}_{\text{enc}}, \mathbf{w}_{\text{dec}}\}$ the union of parameters of the encoder and decoder. The Bayesian treatment of AEs dictates that a prior distribution $p(\mathbf{w})$ is placed over all parameters of f_{enc} and f_{dec} , and that this prior knowledge is transformed into a posterior distribution by means of Bayes’ theorem,

$$p(\mathbf{w} | \mathbf{x}) = \frac{p(\mathbf{x} | \mathbf{w})p(\mathbf{w})}{p(\mathbf{x})}, \quad (1)$$

where $p(\mathbf{x} | \mathbf{w})$ is the conditional likelihood that factorizes as $p(\mathbf{x} | \mathbf{w}) = \prod_{n=1}^N p(\mathbf{x}_n | \mathbf{w})$. Note that each conditional likelihood term is determined by the model architecture, the choice of \mathbf{w} , and the input \mathbf{x}_n , but in order to keep the notation uncluttered, we write them simply as $p(\mathbf{x}_n | \mathbf{w})$.

Likelihood model. In the Bayesian scheme, the prior and likelihood are both modeling choices. Before giving an in-depth treatment on priors for BAEs in the next section, we briefly discuss the likelihood, which can be chosen according to the type of data. In our experiments, we mainly investigate image datasets, where pixel values are normalized in the $[0, 1]$ range. Therefore, we rely on the *continuous Bernoulli* distribution [39]:

$$p(\mathbf{x}_n | \mathbf{w}) = \prod_{i=1}^D K(\lambda_i) \lambda_i^{\mathbf{x}_{n,i}} (1 - \lambda_i)^{1 - \mathbf{x}_{n,i}} := p(\mathbf{x}_n | \hat{\mathbf{x}}_n), \quad (2)$$

where $K(\lambda_i)$ is a properly defined normalization constant [39] and $\lambda_i = f_i(\mathbf{x}_n; \mathbf{w}) = \hat{\mathbf{x}}_{n,i} \in [0, 1]$ is the i -th output from the BAE given the input \mathbf{x}_n . We note that, as $\hat{\mathbf{x}}_n$ depends deterministically on \mathbf{w} , we will use the above expression to refer to both $p(\mathbf{x}_n | \mathbf{w})$ and $p(\mathbf{x}_n | \hat{\mathbf{x}}_n)$, where the latter term will be of crucial importance when we define the functional prior induced over the reconstruction $\hat{\mathbf{x}}$.

Inference. Although the posterior of BAEs is analytically intractable, it can be approximated by variational methods or using MCMC sampling. Within the large family of approximate Bayesian inference schemes, SGHMC [11] allows us to sample from the true posterior by efficiently simulating a Hamiltonian system [49]. Differently from more traditional methods, SGHMC can scale up to large datasets by relying on noisy but unbiased estimates of the potential energy function $U(\mathbf{w}) = -\sum_{n=1}^N \log p(\mathbf{x}_n | \mathbf{w}) - \log p(\mathbf{w})$. These can be computed by considering a mini-batch of size M of the data and approximating $\sum_{n=1}^N \log p(\mathbf{x}_n | \mathbf{w}) \approx \frac{N}{M} \sum_{j \in \mathcal{I}_M} \log p(\mathbf{x}_j | \mathbf{w})$, where \mathcal{I}_M is a set of M random indices. More details on SGHMC can be found in the Appendix.

Pathologies of standard priors. The choice of the prior is important for the Bayesian treatment of any model as it characterizes the hypothesis space [42, 45]. Specifically for BAEs, one should note that placing a prior on the parameters of the encoder and decoder has an implicit effect on the prior over the network output (i.e. the reconstruction). In addition, the highly nonlinear nature of these models implies that interpreting the effect of the architecture is theoretically intractable and practically challenging. Several works argue that a vague prior such as $\mathcal{N}(0, 1)$ is good enough for some tasks and models, like classification with convolutional neural networks (CNNs) [64].

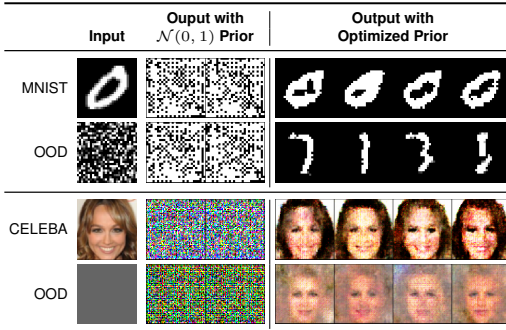


Figure 1: Realizations sampled from different priors given an input image. OOD stands for out-of-distribution.

However, for BAEs this is not enough, as illustrated in Fig. 1. The realizations obtained by sampling weights/biases from a $\mathcal{N}(0, 1)$ prior indicate that this choice provides poor inductive bias. Meanwhile, by encoding better beliefs via an optimized prior, which is the focus of the next section, the samples

can capture main characteristics intrinsic to the data, even when the model is fed with out-of-distribution inputs.

3 Model Selection for Bayesian Autoencoders via Prior Optimization

One of the main advantages of the Bayesian paradigm is that we can incorporate prior knowledge into the model in a principled way. Let us assume a prior distribution $p_\psi(\mathbf{w})$ on the parameters of the AE network, where now we are explicit on the set of (hyper-)parameters that determine the prior, i.e., ψ . Specifying this prior for the BAE is not straightforward due to the complex nonlinear forms of f_{enc} and f_{dec} , which induce a non-trivial effect on the output (functional) prior:

$$p_\psi(\hat{\mathbf{x}}) = \int f(\mathbf{x}; \mathbf{w}) p_\psi(\mathbf{w}) d\mathbf{w}, \quad (3)$$

where $\hat{\mathbf{x}} = f(\mathbf{x}; \mathbf{w})$ is the functional output of the BAE. Although $p_\psi(\hat{\mathbf{x}})$ cannot be evaluated analytically, it is possible to draw samples from it.

Prior parameterization. The only two requirements needed to design a parameterization for the prior are: to be able to (1) draw samples from it and (2) to compute its log-density at any point. The latter is required by many inference algorithms such as SGHMC. We consider a fully-factorized Gaussian prior over weights and biases at layer l :

$$p(w_l) = \mathcal{N}(w_l; \mu_{l_w}, \sigma_{l_w}^2), \quad p(b_l) = \mathcal{N}(b_l; \mu_{l_b}, \sigma_{l_b}^2), \quad (4)$$

Notice that, as we shall see in § 3.2 and § 3.3, in order to estimate our prior hyper-parameters, we will require gradient back-propagation through the stochastic variables w_l and b_l . Thus, we treat these parameters in a deterministic manner by means of the reparameterization trick [32, 55].

3.1 Another route for Bayesian Occam’s razor

A common way to estimate hyper-parameters (i.e., prior parameters ψ) is to rely on the Bayesian Occam’s razor (a.k.a. *empirical Bayes*), which dictates that the marginal likelihood $p_\psi(\mathbf{x})$ should be optimized with respect to ψ . There are countless examples where such simple procedure succeeds in practice [see, e.g., 54]. The marginal likelihood is obtained by marginalizing out the outputs $\hat{\mathbf{x}}$ and the model parameters \mathbf{w} ,

$$p_\psi(\mathbf{x}) = \int p(\mathbf{x} | \hat{\mathbf{x}}) p_\psi(\hat{\mathbf{x}}) d\hat{\mathbf{x}}, \quad (5)$$

where $p(\mathbf{x} | \hat{\mathbf{x}})$ and $p_\psi(\hat{\mathbf{x}})$ are given by Eq. 2 and Eq. 3, respectively. Unfortunately, in our context it is impossible to carry out this optimization due to the intractability of Eq. 5.

Classic results in the statistics literature draw parallels between maximum likelihood estimation (MLE) and KL minimization [2],

$$\arg \max_{\psi} \int \pi(\mathbf{x}) \log p_\psi(\mathbf{x}) d\mathbf{x} = \arg \min_{\psi} \underbrace{\int \pi(\mathbf{x}) \log \frac{\pi(\mathbf{x})}{p_\psi(\mathbf{x})} d\mathbf{x}}_{\text{KL}[\pi(\mathbf{x}) \parallel p_\psi(\mathbf{x})]}, \quad (6)$$

where $\pi(\mathbf{x})$ is the true data distribution. This equivalence provides us with an interesting insight on an alternative view of marginal likelihood optimization as minimization of the divergence between the true data distribution and the marginal $p_\psi(\mathbf{x})$.

This alternative view still does not help us in obtaining a viable optimization strategy, even if we use \mathbf{x} to estimate an empirical $\tilde{\pi}(\mathbf{x})$; the empirical evaluation and optimization of KL divergences is indeed a well-known challenging problem [18], although this is possible (for the KL or any other f -divergence), for example, by leveraging results from convex analysis such as in the convex minimization framework of [51]. However, we can now attempt to replace the intractable KL divergence with another divergence to recover tractability. Inspired by recent works on deriving sensible priors for Bayesian neural networks [60], we employ the Wasserstein distance, which, as we will see later, can be estimated efficiently using samples only, even for high-dimensional distributions.

To summarize: (1) we would like to do prior selection by carrying out type-II MLE; (2) the MLE objective is analytically intractable but the connection with KL minimization allows us to (3) swap the divergence with the Wasserstein distance, yielding a practical framework for choosing priors.

3.2 Matching the marginal distribution to the data distribution via Wasserstein distance minimization

Given the two probability measures π and p_ψ , both defined on \mathbb{R}^D for simplicity, the p -Wasserstein distance between π and p_ψ is given by

$$W_p^p(\pi, p_\psi) = \inf_{\gamma \in \Gamma(\pi, p_\psi)} \int \|\mathbf{x} - \mathbf{x}'\|^p \gamma(\mathbf{x}, \mathbf{x}') d\mathbf{x} d\mathbf{x}', \quad (7)$$

where $\Gamma(\pi, p_\psi)$ is the set of all possible distributions $\gamma(\mathbf{x}, \mathbf{x}')$ such that the marginals are $\pi(\mathbf{x})$ and $p_\psi(\mathbf{x}')$ [62]. While usually analytically unavailable or computationally intractable, for $D = 1$ the distance has a simple closed form solution, that can be easily estimated using samples only [34].

The distributional sliced-Wasserstein distance (DSWD) takes advantage of this result by projecting the estimation of distances for high-dimensional distributions into simpler estimation of multiple distances in one dimension. The projection is done using the Radon transform \mathcal{R} , an operator that maps a generic density function φ defined in \mathbb{R}^D to the set of its integrals over hyperplanes in \mathbb{R}^D ,

$$\mathcal{R}\varphi(t, \boldsymbol{\theta}) := \int \varphi(\mathbf{r}) \delta(t - \mathbf{r}^\top \boldsymbol{\theta}) d\mathbf{r}, \quad \forall t \in \mathbb{R}, \quad \forall \boldsymbol{\theta} \in \mathbb{S}^{D-1}, \quad (8)$$

where \mathbb{S}^{D-1} is the unit sphere in \mathbb{R}^D and $\delta(\cdot)$ is the Dirac delta [24]. Using the Radon transform, for a given direction (or *slice*) $\boldsymbol{\theta}$ we can project the two densities π and p_ψ into one dimension and we can solve the optimal transport problem in this projected space. Furthermore, to avoid unnecessary computations, instead of considering all possible directions in \mathbb{S}^{D-1} , DSWD proposes to find the optimal probability measure of slices $\sigma(\boldsymbol{\theta})$ on the unit sphere \mathbb{S}^{D-1} ,

$$DSW_p(\pi, p_\psi) := \sup_{\sigma \in \mathbb{M}_C} \left(\mathbb{E}_{\sigma(\boldsymbol{\theta})} W_p^p(\mathcal{R}\pi(t, \boldsymbol{\theta}), \mathcal{R}p_\psi(t, \boldsymbol{\theta})) \right)^{1/p}, \quad (9)$$

where, for $C > 0$, \mathbb{M}_C is the set of probability measures σ such that $\mathbb{E}_{\boldsymbol{\theta}, \boldsymbol{\theta}' \sim \sigma} [\boldsymbol{\theta}^\top \boldsymbol{\theta}'] \leq C$ (a constraint that aims to avoid directions to lie in only one small area). The direct computation of DSW_p in Eq. 9 is still challenging but admits an equivalent dual form,

$$\sup_{h \in \mathcal{H}} \left\{ \left(\mathbb{E}_{\bar{\sigma}(\boldsymbol{\theta})} [W_p^p(\mathcal{R}\pi(t, h(\boldsymbol{\theta})), \mathcal{R}p_\psi(t, h(\boldsymbol{\theta}))) \right]^{1/p} - \lambda_C \mathbb{E}_{\boldsymbol{\theta}, \boldsymbol{\theta}' \sim \bar{\sigma}} [|h(\boldsymbol{\theta})^\top h(\boldsymbol{\theta}')|] \right\} + \lambda_C C, \quad (10)$$

where $\bar{\sigma}$ is a uniform distribution in \mathbb{S}^{D-1} , \mathcal{H} is the set of functions $h : \mathbb{S}^{D-1} \rightarrow \mathbb{S}^{D-1}$ and λ_C is a regularization hyper-parameter. The formulation in Eq. 10 is obtained by employing the Lagrangian duality theorem and by reparameterizing $\sigma(\boldsymbol{\theta})$ as push-forward transformation of a uniform measure in \mathbb{S}^{D-1} via h . Now, by parameterizing h using a deep neural network with parameters ϕ , defined as h_ϕ , Eq. 10 becomes an optimization problem with respect to the network parameters. The final step is to approximate the analytically intractable expectations with Monte Carlo integration,

$$\max_{\phi} \left\{ \left[\frac{1}{K} \sum_{i=1}^K [W_p^p(\mathcal{R}\pi(t, h_\phi(\boldsymbol{\theta}_i)), \mathcal{R}p_\psi(t, h_\phi(\boldsymbol{\theta}_i)))] \right]^{1/p} - \frac{\lambda_C}{K^2} \sum_{i,j=1}^K |h_\phi(\boldsymbol{\theta}_i)^\top h_\phi(\boldsymbol{\theta}_j)| \right\} + \lambda_C C,$$

with $\boldsymbol{\theta}_i \sim \bar{\sigma}(\boldsymbol{\theta})$. Finally, we can use stochastic gradient methods to update ϕ and then use the resulting optima for the estimation of the original distance. We encourage the reader to check the detailed explanation of this formulation, including its derivation and some practical considerations for implementation, available in the Appendix.

3.3 Summary

We aim at learning the prior on the BAE parameters by optimizing the marginal $p_\psi(\mathbf{x})$ obtained after integrating out the weights from the joint $p_\psi(\mathbf{x}, \mathbf{w})$. The connection with *empirical Bayes* and KL minimization suggests that we can find the optimal ψ^* by minimizing the KL between the true data distribution $\pi(\mathbf{x})$ and the marginal $p_\psi(\mathbf{x})$. However, matching these two distributions is non-trivial due to their high dimensionality and the unavailability of their densities. To overcome this problem, we propose a sample-based approach using the distributional sliced 2-Wasserstein distance (Eq. 10) as objective:

$$\psi^* = \arg \min_{\psi} [DSW_2(p_\psi(\mathbf{x}), \pi(\mathbf{x}))]. \quad (11)$$

This objective function is flexible and does not require the closed-form of either $p_\psi(\mathbf{x})$ or $\pi(\mathbf{x})$. The only requirement is that we can draw samples from these two distributions. Note that we can sample from $p_\psi(\mathbf{x})$, by first computing $\hat{\mathbf{x}}$ after sampling from $p_\psi(\mathbf{w})$ and then perturbing the generated $\hat{\mathbf{x}}$ by sampling from the likelihood $p(\mathbf{x} | \hat{\mathbf{x}})$. For the continuous Bernoulli likelihood this operation can be implemented by using the reparameterization form that allows to backpropagate gradients [39].

4 Experiments

Competing approaches. We compare our proposal with a wide selection of methods from the literature. For autoencoding methods, we choose the vanilla VAE [32], the β -VAE [26] and WAE (Wasserstein AE) [58]. In addition, we consider models with more complex encoders (VAE + Sylvester flows [61]), generators (2-stage VAE [14]), and priors (VAE + VampPrior [59]). For CELEBA we also include a comparison with Generative Adversarial Networks (GANs), with the vanilla setup of NS-GAN [21, 40] and the more recent DiffAugment-GAN [30, 69]. Finally, we also compare against BAE with the standard $\mathcal{N}(0, 1)$ prior. Unless otherwise stated, all models—including ours—share the same latent dimensionality ($K = 50$). We defer a more detailed description of these models and architectures to the Appendix.

Generative process. Differently from VAEs and other methods, deterministic and Bayesian AEs are not generative models. To generate new samples with BAEs we employ ex-post density estimation over the learned latent space, by fitting a density estimator $p_\vartheta(\mathbf{z})$ to $\{\mathbf{z}_i = \mathbb{E}_{p(\mathbf{w}_{\text{enc}} | \mathbf{x})}[f_{\text{enc}}(\mathbf{x}_i; \mathbf{w}_{\text{enc}})]\}$. In this work, we employ a nonparametric model for density estimation based on Dirichlet Process Mixture Model (DPMM) [7], so that its complexity is automatically adapted to the data; see also [6] for alternative ways to turn AEs into generative models. After estimating $p_\vartheta(\mathbf{z})$, a new sample can be generated by drawing \mathbf{z}_{new} from $p_\vartheta(\mathbf{z})$ and $\hat{\mathbf{x}}_{\text{new}} = \mathbb{E}_{p(\mathbf{w}_{\text{dec}} | \mathbf{x})}[f_{\text{dec}}(\mathbf{z}_{\text{new}}; \mathbf{w}_{\text{dec}})]$.

Evaluation metrics. To evaluate the reconstruction quality, we use the test log-likelihood (LL), which tells us how likely the test targets are generated by the corresponding model. The predictive log-likelihood is a proper scoring rule that depends on both the accuracy of predictions and their uncertainty [20]. To assess the quality of the generated images, instead, we employ the widely used Fréchet Inception Distance (FID) [25]. We note that, as GANs are not inherently equipped with an explicit likelihood model, we only report their FID scores. Finally, all our experiments and evaluations are repeated four times, with different random training splits.

4.1 Analysis of the effect of the prior

To demonstrate the effect of our model selection strategy, we consider scenarios in the small-data regime where the prior might not be necessarily tuned on the training set. In this way we are able to impose inductive bias beyond what is available in the training data. We investigate two cases:

- MNIST [36]: We use 100 examples of the 0 digits to tune the prior. The training set consists of examples of 1-9 digits, whereas the test set contains 10 000 instances of all digits. We aim to demonstrate the ability of our approach to incorporate prior knowledge about completely unseen data with different characteristics into the model.
- FREY-YALE [15]: We use 1 956 examples of FREY faces to optimize the prior. The training set and test set are comprised of YALE faces. We demonstrate the benefit of using a different dataset but from the same domain (e.g. face images) to specify the prior distribution.

Visual inspection. Fig. 2 shows some qualitative results (additional images are available in the Appendix), while Fig. 3 shows the convergence of the Wasserstein distance during prior optimization in our proposal. From a visual inspection we see that, on MNIST, by encoding knowledge about the “0” digit into the prior, the BAE can reconstruct this digit fairly well although we only use “1” to “9” digits for inference (differently from the BAE with standard prior). Similarly, on FREY-YALE, we see that by encoding knowledge from another dataset in the same domain, the optimized prior can impose a softer constraint compared to using directly this dataset for inference. In addition, if we use directly the union of FREY and YALE faces for training (methods denoted with a ★), VAE yields images that are similar to FREY instead of YALE faces, while generated images from BAE with $\mathcal{N}(0, 1)$ prior are of lower quality. This again highlights the advantage of our approach to specifying an informative prior compared to using that data for training. Another important benefit of our Bayesian treatment of AEs is that we can quantify the *uncertainty* for both reconstructed and generated images. The last row of Fig. 2 illustrates the uncertainty estimate corresponding to the BAE with optimized prior on

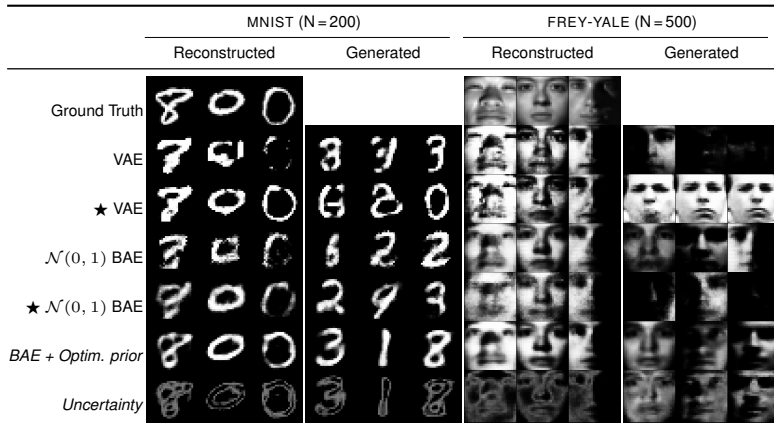


Figure 2: Qualitative evaluation for MNIST and YALE. Here, \star indicates using the union of the training data and the data used to optimize prior to train the model. The last row depicts standard deviation of reconstructed/generated images estimated by BAE using the optimized prior.

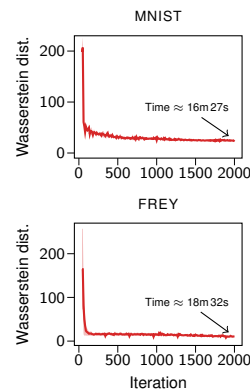


Figure 3: Convergence of the proposed Wasserstein minimization scheme.

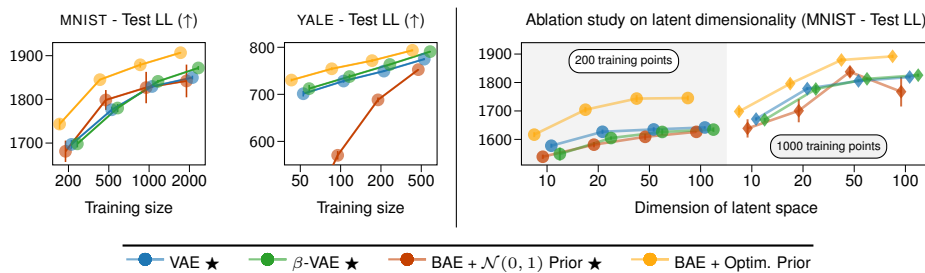


Figure 4: Test log-likelihood (LL) of MNIST and YALE. *Left:* test LL as a function of training size; *Right:* test LL as a function of latent dimensionality.

MNIST and YALE datasets. Our model exhibits increased uncertainty for semantically and visually challenging pixels such as the left part of the second “0” digit image in the MNIST example. We also observe that the uncertainty is greater for generated images compared to reconstructed images as illustrated in the YALE example. This is reasonable because the reconstruction process is guided by the input data rather than synthesizing new data according to a random latent code.

Visualization of inductive bias on MNIST. To have an intuition of the inductive bias induced by the optimized prior, we visualize a low-dimensional projection of parameters sampled from the prior and the posterior [28]. As we see in Fig. 5, the hypothesis space induced by the $\mathcal{N}(0, 1)$ prior is huge, compared to where the true solution should lie. Effectively this is another visualization of the famous Bayesian Occam’s razor plot by David MacKay [43], where the model has very high complexity and poor inductive biases. On the other hand, by considering our proposal to do *model selection*, the hypothesis space of the optimized prior is reduced to regions close to the full posterior. Additional visualizations are available in the Appendix.

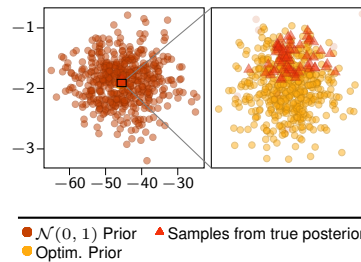


Figure 5: Visualization in 2D of samples from priors and posteriors of BAE’s parameters. The setup is the same as before with MNIST.

Quantitative evaluation. For a quantitative analysis we rely on Fig. 4, where we study the effect on the reconstruction quality of different training sizes (on the *left*) and different latent dimensions (on the *right*). Since we observed that the results of VAE variants are not significantly different, we only show the results for β -VAE and we leave the extended results to the Appendix. From this experiment we can draw important conclusions. The BAE with optimized priors clearly outperforms the competing methods (and the BAE with standard prior) in the inference task for all training sizes,

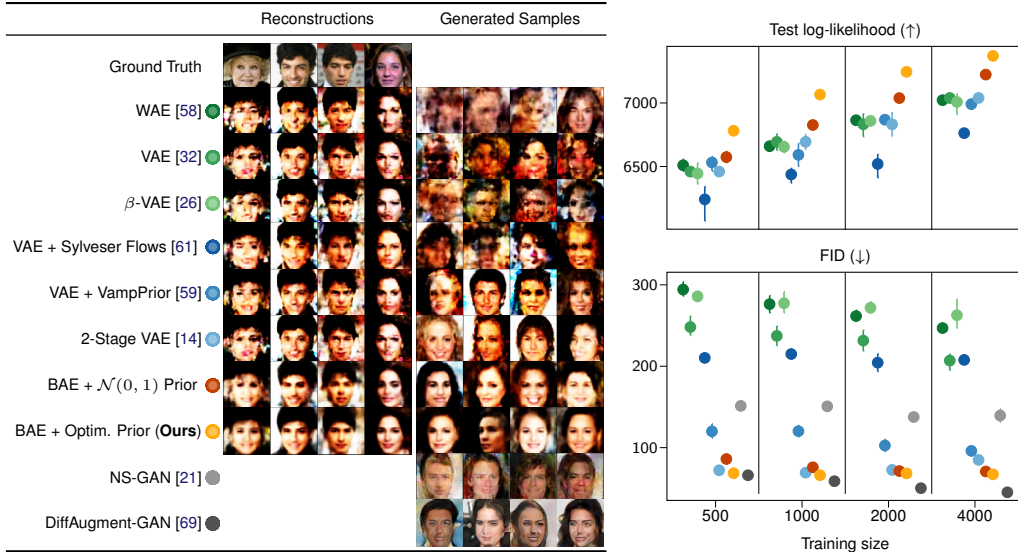


Figure 6: Qualitative (*left*) and quantitative evaluation (*right*) on CELEBA. The markers and bars represent the means and one standard deviations, respectively. In the (*left*) figure, the sizes of training data and the data for optimizing prior are 500 and 1000, respectively. The higher the log-likelihood (LL) and the lower FID the better.

with slightly diminishing effect for larger sets, as expected. Also, this pattern is true when looking at different latent dimensions (Fig. 4, *left*), where regardless of the dimensionality of the latent space, BAEs with optimized priors deliver higher performances.

4.2 Reconstruction and generation of CELEBA

We now look at a more challenging benchmark, the CELEBA dataset [38]. For our proposal, we use 1 000 examples that are randomly chosen from the original training set to learn the prior distribution. The test set consists of about 20 000 images. The goal of this experiment is to evaluate whether sacrificing part of the training data to specify a good prior is beneficial when compared to using that data for training the model. Fig. 6 shows qualitative results for the competing methods, their corresponding test LLs and FIDs for different training dataset sizes. In terms of test log-likelihoods (LLs) (Fig. 6, *top right*), we observe two clear patterns: (i) that BAE approaches perform considerably better than other methods and (ii) the VAE with Sylvester flows performs consistently poor across dataset sizes. This latter observation indicates that having a more expressive posterior for the encoder is not helpful when considering the small training sizes used in our experiments. More importantly, we see that the BAE using the optimized prior significantly outperforms other methods despite using less data for inference. These results largely agree with the quality of the reconstructions (first column of images in Fig. 6, *left*) in that BAE methods provide more visually appealing reconstructions when compared to other approaches.

We now evaluate the quality of the generated images (second column of images in Fig. 6, *left*) along with their FID scores [25]. Visually, it is clear that images generated from VAEs (standard, β , Sylvester and WAE) are very poor. This failure may originate from the fact that the aggregated posterior distribution of the encoder is not aligned with the prior on the latent space. This problem is more prominent in the case of small training data, where the encoder is not well-trained. The VampPrior tackles this problem by explicitly modeling the aggregated posterior, while 2-stage VAE uses another VAE to estimate the density of the learned latent space. By reducing the effect of the aggregated posterior mismatch, these strategies improve the quality of the generated images remarkably. These results are consistent with their corresponding FID scores (Fig. 6, *bottom right*) where we also see that BAE using the optimized prior consistently outperforms all variants of VAEs and NS-GAN. Finally, we see that DiffAugment-GAN, with the exception of using a training size of 500, yields better FID scores. However, this is not surprising as this model uses much more complex network architectures [30], combined with a powerful differentiable augmentation scheme. More importantly, it is clear that with few training samples our method generates more semantically meaningful images than all other approaches, including DiffAugment-GAN.

4.3 Prior adjustment versus posterior tempering

We have shown that the proposed framework for adjusting the prior is compatible with standard Bayesian practices, as it emulates type-II maximum likelihood. In other words, the distribution fitting that we induce by means of Wasserstein distance minimization relates to the marginal output of BAEs, very much in the same spirit of marginal likelihood maximization. The distribution is fit considering *all* possible functions, when marginalized through the likelihood, creating an implicit regularization effect. Our scheme does not give more weight to particular training instances, but it simply restricts the hypothesis space. This is unlike *posterior tempering* [1, 28, 63, 66, 67], which is commonly defined as $p_{\tau}(\mathbf{w} | \mathbf{x}) \propto p(\mathbf{x} | \mathbf{w})^{1/\tau} p(\mathbf{w})$, where $\tau > 0$ is a *temperature* value. With $\tau < 1$, tempering is known to improve performance in the case of small training data and using miss-specified priors, but it corresponds to artificially sharpening the posterior by over-counting the data τ times.

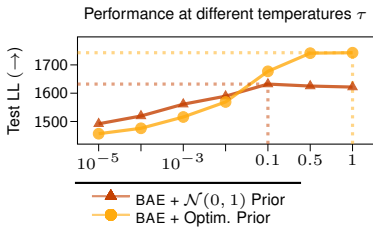


Figure 8: Test performance for temperature scaling with different priors. The dotted lines indicate the best performance.

5 Conclusions

In this work, we have reconsidered the Bayesian treatment of autoencoders (AE) in light of recent advances in Bayesian neural networks. We have addressed the main challenge of BAEs, so that they can be rendered as viable alternative to generative models such as VAEs. More specifically, we have found that the main limitation of BAEs lies in the difficulty of specifying meaningful priors in the context of highly-structured data, which is ubiquitous in modern machine learning applications. Consequently, we have proposed to specify priors over the autoencoder weights by means of a novel optimization of prior hyper-parameters. Inspired by connections with marginal likelihood optimization, we derived a practical and efficient optimization framework, based on the minimization of the distributional sliced-Wasserstein distance between the distribution induced by the BAE and the data generating distribution. The resulting hyper-parameter optimization strategy leads to a novel way to perform model selection for BAEs, and we showed its advantages in an extensive experimental campaign.

Limitations and ethical concerns. Even if theoretically justified and empirically verified with extensive experimentation, our proposal for model selection still remains a *proxy* to the true marginal likelihood maximization. The DSWD formulation has nice properties of asymptotic convergence and computational tractability, but it may represent only one of the possible solutions. At the same time, we stress that the current literature does not cover this problem of BAEs at all, and we believe our approach is a considerable step towards the development of practical Bayesian methods for representation learning in modern applications characterized by large-scale structured data (including tabular and graph data, which are currently not covered). At the same time, the accessibility to these models to a wider audience and different kind of data might help to widespread harmful applications, which is a concern shared among all generative modeling approaches. An ethical analysis of the consequences of Bayesian priors in unsupervised learning scenarios is also worth an in-depth investigation, which goes beyond the scope of this work.

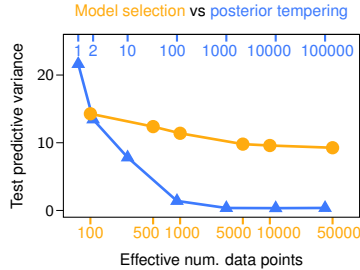


Figure 7: Average test predictive variance as a function of the number of data points used to optimize the prior, and the temperature (i.e. how many times the data points are over-counted).

To demonstrate the differences with our proposal, we setup a comparison on MNIST. In the empirical comparison of Fig. 7, we consider different temperatures and different sets of data points used to optimize the prior. As expected, the tempered posterior quickly collapses on the mode, while the posterior after our treatment retains a sufficiently constant variance, regardless of the number of data points used. It is also interesting to notice that with the $\mathcal{N}(0, 1)$ prior, the best temperature is $\tau = 0.1$, while for our approach that optimizes the prior is $\tau = 1$, further confirming that the model now is well specified (Fig. 8).

Acknowledgments and Disclosure of Funding

MF gratefully acknowledges support from the AXA Research Fund and the Agence Nationale de la Recherche (grant ANR-18-CE46-0002 and ANR-19-P3IA-0002).

References

- [1] L. Aitchison. A Statistical Theory of Cold Posteriors in Deep Neural Networks. In *International Conference on Learning Representations*, 2021.
- [2] H. Akaike. Information Theory and an Extension of the Maximum Likelihood Principle. In *2nd International Symposium on Information Theory, 1973*, pages 268–281. Publishing House of the Hungarian Academy of Sciences, 1973.
- [3] P. Baldi and K. Hornik. Neural Networks and Principal Component Analysis: Learning from Examples Without Local Minima. *Neural networks*, 2(1):53–58, 1989.
- [4] M. Bauer and A. Mnih. Resampled Priors for Variational Autoencoders. In *The 22nd International Conference on Artificial Intelligence and Statistics, AISTATS 2019, 16-18 April 2019, Naha, Okinawa, Japan*, volume 89 of *Proceedings of Machine Learning Research*, pages 66–75. PMLR, 2019.
- [5] Y. Bengio, A. Courville, and P. Vincent. Representation Learning: A Review and New Perspectives. *IEEE Transactions on Pattern Analysis and Machine Intelligence*, 35(8):1798–1828, 2013.
- [6] Y. Bengio, L. Yao, G. Alain, and P. Vincent. Generalized Denoising Auto-Encoders as Generative Models. In *Advances in Neural Information Processing Systems 26: 27th Annual Conference on Neural Information Processing Systems 2013. Proceedings of a meeting held December 5-8, 2013, Lake Tahoe, Nevada, United States*, pages 899–907, 2013.
- [7] D. M. Blei and M. I. Jordan. Variational Inference for Dirichlet Process Mixtures. *Bayesian Analysis*, 1(1):121 – 143, 2006.
- [8] V. Böhm and U. Seljak. Probabilistic Auto-Encoder. *arXiv preprint arXiv:2006.05479*, 2020.
- [9] N. Bonneel, J. Rabin, G. Peyré, and H. Pfister. Sliced and Radon Wasserstein Barycenters of Measures. *Journal of Mathematical Imaging and Vision*, 51(1):22–45, 2015.
- [10] Y. Burda, R. B. Grosse, and R. Salakhutdinov. Importance Weighted Autoencoders. In *4th International Conference on Learning Representations, ICLR 2016, San Juan, Puerto Rico, May 2-4, 2016, Conference Track Proceedings*, 2016.
- [11] T. Chen, E. Fox, and C. Guestrin. Stochastic Gradient Hamiltonian Monte Carlo. In *Proceedings of the 31st International Conference on Machine Learning, ICML 2014*, Proceedings of Machine Learning Research, pages 1683–1691, Beijing, China, 22–24 Jun 2014. PMLR.
- [12] X. Chen, D. P. Kingma, T. Salimans, Y. Duan, P. Dhariwal, J. Schulman, I. Sutskever, and P. Abbeel. Variational Lossy Autoencoder. In *5th International Conference on Learning Representations, ICLR 2017, Toulon, France, April 24-26, 2017, Conference Track Proceedings*. OpenReview.net, 2017.
- [13] G. W. Cottrell, P. Munro, and D. Zipser. Image Compression by Back Propagation: A Demonstration of Extensional Programming. *Models of Cognition*, pages 208–240, 1989.
- [14] B. Dai and D. Wipf. Diagnosing and Enhancing VAE Models. In *International Conference on Learning Representations*, 2019.
- [15] Z. Dai, A. C. Damianou, J. González, and N. D. Lawrence. Variational Auto-encoded Deep Gaussian Processes. In *4th International Conference on Learning Representations, ICLR 2016, San Juan, Puerto Rico, May 2-4, 2016, Conference Track Proceedings*, 2016.
- [16] E. A. Daxberger and J. M. Hernández-Lobato. Bayesian Variational Autoencoders for Unsupervised Out-of-Distribution Detection. *arXiv preprint arXiv:1912.05651*, 2019.
- [17] L. Dinh, J. Sohl-Dickstein, and S. Bengio. Density estimation using real NVP. In *5th International Conference on Learning Representations, ICLR 2017, Toulon, France, April 24-26, 2017, Conference Track Proceedings*. OpenReview.net, 2017.
- [18] D. Flam-Shepherd, J. Requeima, and D. Duvenaud. Mapping Gaussian Process Priors to Bayesian Neural Networks. In *NeurIPS workshop on Bayesian Deep Learning*, 2017.
- [19] P. Ghosh, M. S. M. Sajjadi, A. Vergari, M. Black, and B. Scholkopf. From Variational to Deterministic Autoencoders. In *International Conference on Learning Representations*, 2020.
- [20] T. Gneiting and A. E. Raftery. Strictly Proper Scoring Rules, Prediction, and Estimation. *Journal of the American statistical Association*, 102(477):359–378, 2007.

- [21] I. Goodfellow, J. Pouget-Abadie, M. Mirza, B. Xu, D. Warde-Farley, S. Ozair, A. Courville, and Y. Bengio. Generative Adversarial Nets. In *Advances in Neural Information Processing Systems*, volume 27. Curran Associates, Inc., 2014.
- [22] D. Hafner, D. Tran, T. P. Lillicrap, A. Irpan, and J. Davidson. Noise Contrastive Priors for Functional Uncertainty. In *Proceedings of the 35th Conference on Uncertainty in Artificial Intelligence, UAI 2019*, page 332, Tel Aviv, Israel, 22-25 July 2019 2019. AUAI Press.
- [23] N. Halko, P. Martinsson, and J. A. Tropp. Finding Structure with Randomness: Probabilistic Algorithms for Constructing Approximate Matrix Decompositions. *SIAM Rev.*, 53(2):217–288, 2011.
- [24] S. Helgason. *Integral Geometry and Radon Transforms*. Springer Science & Business Media, 2010.
- [25] M. Heusel, H. Ramsauer, T. Unterthiner, B. Nessler, and S. Hochreiter. GANs Trained by a Two Time-Scale Update Rule Converge to a Local Nash Equilibrium. In *Advances in Neural Information Processing Systems 30: Annual Conference on Neural Information Processing Systems 2017, December 4-9, 2017, Long Beach, CA, USA*, pages 6626–6637, 2017.
- [26] I. Higgins, L. Matthey, A. Pal, C. Burgess, X. Glorot, M. Botvinick, S. Mohamed, and A. Lerchner. beta-VAE: Learning Basic Visual Concepts with a Constrained Variational Framework. In *5th International Conference on Learning Representations, ICLR 2017, Toulon, France, April 24-26, 2017, Conference Track Proceedings*. OpenReview.net, 2017.
- [27] G. E. Hinton and R. R. Salakhutdinov. Reducing the Dimensionality of Data with Neural Networks. *Science*, 313(5786):504–507, 2006.
- [28] P. Izmailov, W. Maddox, P. Kirichenko, T. Garipov, D. P. Vetrov, and A. G. Wilson. Subspace Inference for Bayesian Deep Learning. In *Proceedings of the Thirty-Fifth Conference on Uncertainty in Artificial Intelligence, UAI 2019, Tel Aviv, Israel, July 22-25, 2019*, volume 115 of *Proceedings of Machine Learning Research*, pages 1169–1179. AUAI Press, 2019.
- [29] P. Izmailov, S. Vikram, M. D. Hoffman, and A. G. Wilson. What Are Bayesian Neural Network Posteriors Really Like? In *Proceedings of the 38th International Conference on Machine Learning, ICML 2021, 18-24 June 2021, Virtual Event, 2021*.
- [30] T. Karras, S. Laine, M. Aittala, J. Hellsten, J. Lehtinen, and T. Aila. Analyzing and Improving the Image Quality of StyleGAN. In *2020 IEEE/CVF Conference on Computer Vision and Pattern Recognition, CVPR 2020, Seattle, WA, USA, June 13-19, 2020*, pages 8107–8116. IEEE, 2020.
- [31] D. P. Kingma and J. Ba. Adam: A Method for Stochastic Optimization. In *International Conference on Learning Representations*, 2015.
- [32] D. P. Kingma and M. Welling. Auto-Encoding Variational Bayes. In *International Conference on Learning Representations*, 2014.
- [33] D. P. Kingma and M. Welling. An Introduction to Variational Autoencoders. *Foundations and Trends in Machine Learning*, 12(4):307–392, 2019.
- [34] S. Kolouri, K. Nadjahi, U. Simsekli, R. Badeau, and G. K. Rohde. Generalized Sliced Wasserstein Distances. In *Advances in Neural Information Processing Systems 32: Annual Conference on Neural Information Processing Systems 2019, NeurIPS 2019, December 8-14, 2019, Vancouver, BC, Canada*, pages 261–272, 2019.
- [35] N. D. Lawrence. Probabilistic Non-linear Principal Component Analysis with Gaussian Process Latent Variable Models. *Journal of Machine Learning Research*, 6:1783–1816, 2005.
- [36] Y. Lecun, L. Bottou, Y. Bengio, and P. Haffner. Gradient-Based Learning Applied to Document Recognition. *Proceedings of the IEEE*, 86(11):2278–2324, 1998.
- [37] H. Li, Z. Xu, G. Taylor, C. Studer, and T. Goldstein. Visualizing the Loss Landscape of Neural Nets. In *Advances in Neural Information Processing Systems 31: Annual Conference on Neural Information Processing Systems 2018, NeurIPS 2018, December 3-8, 2018, Montréal, Canada*, pages 6391–6401, 2018.
- [38] Z. Liu, P. Luo, X. Wang, and X. Tang. Deep Learning Face Attributes in the Wild. In *2015 IEEE International Conference on Computer Vision, ICCV 2015, Santiago, Chile, December 7-13, 2015*, pages 3730–3738. IEEE Computer Society, 2015.
- [39] G. Loaiza-Ganem and J. P. Cunningham. The Continuous Bernoulli: Fixing a Pervasive Error in Variational Autoencoders. In *Advances in Neural Information Processing Systems 32: Annual Conference on Neural Information Processing Systems 2019, NeurIPS 2019, December 8-14, 2019, Vancouver, BC, Canada*, pages 13266–13276, 2019.
- [40] M. Lucic, K. Kurach, M. Michalski, S. Gelly, and O. Bousquet. Are GANs Created Equal? A Large-Scale Study. In *Advances in Neural Information Processing Systems 31: Annual Conference on Neural Information Processing Systems 2018, NeurIPS 2018, December 3-8, 2018, Montréal, Canada*, pages 698–707, 2018.

- [41] D. J. MacKay and M. N. Gibbs. Density Networks. *Statistics and Neural Networks: Advances at the Interface*, pages 129–144, 1999.
- [42] D. J. C. Mackay. *Bayesian Methods for Adaptive Models*. PhD thesis, California Institute of Technology, USA, 1992. UMI Order No. GAX92-32200.
- [43] D. J. C. Mackay. *Information Theory, Inference and Learning Algorithms*. Cambridge University Press, first edition edition, June 2003.
- [44] W. J. Maddox, P. Izmailov, T. Garipov, D. P. Vetrov, and A. G. Wilson. A Simple Baseline for Bayesian Uncertainty in Deep Learning. In *Advances in Neural Information Processing Systems 32: Annual Conference on Neural Information Processing Systems 2019, NeurIPS 2019, December 8-14, 2019, Vancouver, BC, Canada*, pages 13132–13143, 2019.
- [45] I. Murray and Z. Ghahramani. A Note on the Evidence and Bayesian Occam’s Razor. Technical Report GCNU-TR 2005-003, Gatsby Computational Neuroscience Unit, University College London, 2005.
- [46] E. T. Nalisnick. *On Priors for Bayesian Neural Networks*. PhD thesis, University of California, Irvine, USA, 2018.
- [47] E. T. Nalisnick, J. Gordon, and J. M. Hernández-Lobato. Predictive Complexity Priors. In *The 24th International Conference on Artificial Intelligence and Statistics, AISTATS 2021, April 13-15, 2021, Virtual Event*, volume 130 of *Proceedings of Machine Learning Research*, pages 694–702. PMLR, 2021.
- [48] E. T. Nalisnick and P. Smyth. Stick-Breaking Variational Autoencoders. In *5th International Conference on Learning Representations, ICLR 2017, Toulon, France, April 24-26, 2017, Conference Track Proceedings*. OpenReview.net, 2017.
- [49] R. M. Neal. *MCMC Using Hamiltonian Dynamics*, chapter 5. CRC Press, 2011.
- [50] K. Nguyen, N. Ho, T. Pham, and H. Bui. Distributional Sliced-Wasserstein and Applications to Generative Modeling. In *International Conference on Learning Representations*, 2021.
- [51] X. Nguyen, M. J. Wainwright, and M. I. Jordan. Estimating Divergence Functionals and the Likelihood Ratio by Convex Risk Minimization. *IEEE Transactions on Information Theory*, 56(11):5847–5861, 2010.
- [52] K. Osawa, S. Swaroop, M. E. Khan, A. Jain, R. Eschenhagen, R. E. Turner, and R. Yokota. Practical Deep Learning with Bayesian Principles. In *Advances in Neural Information Processing Systems 32: Annual Conference on Neural Information Processing Systems 2019, NeurIPS 2019, December 8-14, 2019, Vancouver, BC, Canada*, pages 4289–4301, 2019.
- [53] A. Paszke, S. Gross, F. Massa, A. Lerer, J. Bradbury, G. Chanan, T. Killeen, Z. Lin, N. Gimelshein, L. Antiga, A. Desmaison, A. Kopf, E. Yang, Z. DeVito, M. Raison, A. Tejani, S. Chilamkurthy, B. Steiner, L. Fang, J. Bai, and S. Chintala. PyTorch: An Imperative Style, High-Performance Deep Learning Library. In *Advances in Neural Information Processing Systems*, volume 32, pages 8026–8037. Curran Associates, Inc., 2019.
- [54] C. E. Rasmussen and C. Williams. *Gaussian Processes for Machine Learning*. MIT Press, 2006.
- [55] D. J. Rezende, S. Mohamed, and D. Wierstra. Stochastic Backpropagation and Approximate Inference in Deep Generative Models. In *Proceedings of the 31th International Conference on Machine Learning, ICML 2014*, volume 32 of *Proceeding of Machine Learning Research*, pages 1278–1286, Beijing, China, 21-26 June 2014. PMLR.
- [56] J. T. Springenberg, A. Klein, S. Falkner, and F. Hutter. Bayesian Optimization with Robust Bayesian Neural Networks. In *Advances in Neural Information Processing Systems*, volume 29, pages 4134–4142. Curran Associates, Inc., 2016.
- [57] S. Sun, G. Zhang, J. Shi, and R. Grosse. Functional Variational Bayesian Neural Networks. In *International Conference on Learning Representations*, 2019.
- [58] I. Tolstikhin, O. Bousquet, S. Gelly, and B. Schoelkopf. Wasserstein Auto-Encoders. In *International Conference on Learning Representations*, 2018.
- [59] J. M. Tomczak and M. Welling. VAE with a VampPrior. In *International Conference on Artificial Intelligence and Statistics, AISTATS 2018, 9-11 April 2018, Playa Blanca, Lanzarote, Canary Islands, Spain*, volume 84 of *Proceedings of Machine Learning Research*, pages 1214–1223. PMLR, 2018.
- [60] B.-H. Tran, S. Rossi, D. Milios, and M. Filippone. All You Need is a Good Functional Prior for Bayesian Deep Learning. *arXiv preprint arXiv:2011.12829*, 2020.
- [61] R. van den Berg, L. Hasenclever, J. M. Tomczak, and M. Welling. Sylvester Normalizing Flows for Variational Inference. In *Proceedings of the Thirty-Fourth Conference on Uncertainty in Artificial Intelligence, UAI 2018, Monterey, California, USA, August 6-10, 2018*, pages 393–402. AUAI Press, 2018.
- [62] C. Villani. *Optimal Transport: Old and New*, volume 338. Springer Science & Business Media, 2008.

- [63] F. Wenzel, K. Roth, B. S. Veeling, J. Świątkowski, L. Tran, S. Mandt, J. Snoek, T. Salimans, R. Jenatton, and S. Nowozin. How Good is the Bayes Posterior in Deep Neural Networks Really? In *Proceeding of the 37th International Conference on Machine Learning, ICML 2020*, Virtual, 25-30 June 2020.
- [64] A. G. Wilson and P. Izmailov. Bayesian Deep Learning and a Probabilistic Perspective of Generalization. In *Advances in Neural Information Processing Systems 33: Annual Conference on Neural Information Processing Systems 2020, NeurIPS 2020, December 6-12, 2020, virtual*, 2020.
- [65] W. Yang, L. Lorch, M. A. Graule, H. Lakkaraju, and F. Doshi-Velez. Incorporating Interpretable Output Constraints in Bayesian Neural Networks. In *Advances in Neural Information Processing Systems 33: Annual Conference on Neural Information Processing Systems 2020, NeurIPS 2020, December 6-12, 2020, virtual*, 2020.
- [66] C. Zeno, I. Golan, A. Pakman, and D. Soudry. Why Cold Posteriors? On the Suboptimal Generalization of Optimal Bayes Estimates. In *Third Symposium on Advances in Approximate Bayesian Inference*, 2021.
- [67] G. Zhang, S. Sun, D. Duvenaud, and R. B. Grosse. Noisy Natural Gradient as Variational Inference. In *Proceedings of the 35th International Conference on Machine Learning, ICML 2018, Stockholmsmässan, Stockholm, Sweden, July 10-15, 2018*, volume 80 of *Proceedings of Machine Learning Research*, pages 5847–5856. PMLR, 2018.
- [68] R. Zhang, C. Li, J. Zhang, C. Chen, and A. G. Wilson. Cyclical Stochastic Gradient MCMC for Bayesian Deep Learning. In *8th International Conference on Learning Representations, ICLR 2020, Addis Ababa, Ethiopia, April 26-30, 2020*. OpenReview.net, 2020.
- [69] S. Zhao, Z. Liu, J. Lin, J. Zhu, and S. Han. Differentiable Augmentation for Data-Efficient GAN Training. In *Advances in Neural Information Processing Systems 33: Annual Conference on Neural Information Processing Systems 2020, NeurIPS 2020, December 6-12, 2020, virtual*, 2020.

A Derivation of Distributional Sliced-Wasserstein Distance

In this section, we review some key results on the Wasserstein distance. Given two probability measures π, ρ , both defined on \mathbb{R}^D for simplicity, the p -Wasserstein distance between π and ρ is given by

$$W_p^p(\pi, \rho) = \inf_{\gamma \in \Gamma(\pi, \rho)} \int \|\mathbf{x} - \mathbf{y}\|^p \gamma(\mathbf{x}, \mathbf{y}) d\mathbf{x}d\mathbf{y}, \quad (12)$$

where $\Gamma(\pi, \rho)$ is the set of all possible distributions $\gamma(\mathbf{x}, \mathbf{y})$ such that the marginals are $\pi(\mathbf{x})$ and $\rho(\mathbf{y})$ [62]. While usually analytically unavailable, for $D = 1$ the distance has the following closed form solution,

$$W_p^p(\pi, \rho) = \int_0^1 |F_\pi^{-1}(z) - F_\rho^{-1}(z)|^p dz, \quad (13)$$

where F_π and F_ρ are the cumulative density functions (CDFs) of π and ρ , respectively.

A.1 (Distributional) Sliced-Wasserstein Distance

The main idea underlying the DSWD is to project the challenging estimation of distances for high-dimensional distributions into simpler estimation of multiple distances in one dimension, which all have closed-form solution (Eq. 13). The projection is done using the Radon transform \mathcal{R} , an operator that maps a density function φ defined in \mathbb{R}^D to the set of its integrals over hyperplanes in \mathbb{R}^D ,

$$\mathcal{R}\varphi(t, \boldsymbol{\theta}) := \int \varphi(\mathbf{z}) \delta(t - \mathbf{z}^\top \boldsymbol{\theta}) d\mathbf{z}, \quad \forall t \in \mathbb{R}, \quad \forall \boldsymbol{\theta} \in \mathbb{S}^{D-1}, \quad (14)$$

where \mathbb{S}^{D-1} is the unit sphere in \mathbb{R}^D and $\delta(\cdot)$ is the Dirac delta [24]. Using the Radon transform, for a given $\boldsymbol{\theta}$ we can project the two densities π and ρ into one dimension,

$$W_p^p(\pi, \rho) = \int_{\mathbb{S}^{D-1}} W_p^p(\mathcal{R}\pi(t, \boldsymbol{\theta}), \mathcal{R}\rho(t, \boldsymbol{\theta})) d\boldsymbol{\theta} \approx \frac{1}{K} \sum_{i=1}^K W_p^p(\mathcal{R}\pi(t, \boldsymbol{\theta}_i), \mathcal{R}\rho(t, \boldsymbol{\theta}_i)), \quad (15)$$

where the approximation comes from using Monte-Carlo integration by sampling $\boldsymbol{\theta}_i$ uniformly in \mathbb{S}^{D-1} [9]. While having significant computational advantages, this approach might require to draw many unimportant projections that are computationally exhausting and that provide a minimal improvement on the overall distance approximation.

The *distributional sliced-Wasserstein distance* (DSW) [50] solves this issue by finding the optimal probability measure of slices $\sigma(\boldsymbol{\theta})$ on the unit sphere \mathbb{S}^{D-1} and it's defined as follows,

$$DSW_p(\pi, \rho; C) := \sup_{\sigma \in \mathbb{M}_C} \left(\mathbb{E}_{\sigma(\boldsymbol{\theta})} W_p^p(\mathcal{R}\pi(t, \boldsymbol{\theta}), \mathcal{R}\rho(t, \boldsymbol{\theta})) \right)^{1/p}, \quad (16)$$

where, for $C > 0$, \mathbb{M}_C is the set of probability measures σ such that $\mathbb{E}_{\boldsymbol{\theta}, \boldsymbol{\theta}' \sim \sigma} [\boldsymbol{\theta}^\top \boldsymbol{\theta}'] \leq C$ (a constraint that aims to avoid directions to lie in only one small area). Critically, the definition of DSWD in Eq. 16 does not suffer from the curse of dimensionality, indeed [50] showed that the statistical error of this estimation scales down with $C_D \cdot n^{-\frac{1}{2}}$, where C_D is a constant depending on dimension D . Furthermore, while generally we have that $DSW_p(\pi, \rho) \leq W_p(\pi, \rho)$, it can be proved that under mild assumptions on C , the two distances are topological equivalent, i.e. converging in distribution on DSW_p implies the convergence on W_p [see Theorem 2 in 50].

The direct computation of DSW_p in Eq. 16 is still challenging but it admits an equivalent dual form,

$$\sup_{h \in \mathcal{H}} \left\{ \left(\mathbb{E}_{\bar{\sigma}(\boldsymbol{\theta})} [W_p^p(\mathcal{R}\pi(t, h(\boldsymbol{\theta})), \mathcal{R}\rho(t, h(\boldsymbol{\theta}))) \right] \right)^{1/p} - \lambda_C \mathbb{E}_{\boldsymbol{\theta}, \boldsymbol{\theta}' \sim \bar{\sigma}} [|h(\boldsymbol{\theta})^\top h(\boldsymbol{\theta}')|] \right\} + \lambda_C C, \quad (17)$$

where $\bar{\sigma}$ is a uniform distribution in \mathbb{S}^{D-1} , \mathcal{H} is a class of all Borel measurable functions $\mathbb{S}^{D-1} \rightarrow \mathbb{S}^{D-1}$ and λ_C is a regularization hyper-parameter. The formulation in Eq. 17 is obtained by employing the Lagrangian duality theorem and by reparameterizing $\sigma(\boldsymbol{\theta})$ as push-forward transformation of

a uniform measure in \mathbb{S}^{D-1} via h . Now, by parameterizing h using a deep neural network¹ with parameters ϕ , defined as h_ϕ , Eq. 17 becomes an optimization problem with respect to the network parameters. The final step is to approximate the analytically intractable expectations with Monte Carlo integration,

$$DSW_p(\pi, \rho) \approx \max_{\phi} \left\{ \left[\frac{1}{K} \sum_{i=1}^K [W_p^p(\mathcal{R}\pi(t, h_\phi(\boldsymbol{\theta}_i)), \mathcal{R}\rho(t, h_\phi(\boldsymbol{\theta}_i)))] \right]^{1/p} - \frac{\lambda_C}{K^2} \sum_{i,j=1}^K |h_\phi(\boldsymbol{\theta}_i)^\top h_\phi(\boldsymbol{\theta}_j)| + \lambda_C C \right\}, \quad (18)$$

where $\boldsymbol{\theta}_i$ are uniform samples from the unit sphere \mathbb{S}^{D-1} and $\forall t \in \mathbb{R}$. Finally, we can use stochastic gradient methods to update ϕ and then use the resulting optima for the estimation of the original distance.

B Numerical Implementation of Sliced-Wasserstein Distance

B.1 Wasserstein distance between two empirical 1D distributions

The Wasserstein distance between two one-dimensional distributions π and ρ is defined as in Eq. 13. The integral in this equation can be numerically estimated by using the midpoint Riemann sum:

$$\int_0^1 |F_\pi^{-1}(z) - F_\rho^{-1}(z)|^p dz \approx \frac{1}{M} \sum_{m=1}^M |F_\pi^{-1}(z_m) - F_\rho^{-1}(z_m)|^p, \quad (19)$$

where $z_m = \frac{2m-1}{M}$, M is the number of points used to approximate the integral. If we only have samples from the distributions, $x_m \sim \pi$ and $y_m \sim \rho$, we can obtain the empirical densities as follows

$$\pi(x) \approx \pi_M(x) = \frac{1}{M} \sum_{m=1}^M \delta(x - x_m), \quad (20)$$

$$\rho(y) \approx \rho_M(y) = \frac{1}{M} \sum_{m=1}^M \delta(y - y_m), \quad (21)$$

where δ is the Dirac delta function. The corresponding empirical cumulative density functions are

$$F_\pi(z) \approx F_{\pi,M}(z) = \frac{1}{M} \sum_{m=1}^M u(z - x_m), \quad (22)$$

$$F_\rho(z) \approx F_{\rho,M}(z) = \frac{1}{M} \sum_{m=1}^M u(z - y_m), \quad (23)$$

where M is the number of samples, $u(\cdot)$ is the step function.

Calculating the Wasserstein distance with the empirical distribution function is computationally attractive. To do that, we first sort x_m s in an ascending order, such that $x_{i[m]} \leq x_{i[m+1]}$, where $i[m]$ is the index of the sorted x_m s. It is straightforward to show that $F_{\pi,M}^{-1}(z_m) = x_{i[m]}$. Thus, the Wasserstein distance can be approximated as follows

$$W_p^p(\pi, \rho) \approx \frac{1}{M} \sum_{m=1}^M |x_{i[m]} - y_{j[m]}|^p. \quad (24)$$

B.2 Slicing empirical distribution

According to the equation Eq. 14, the marginal densities (i.e. slices) of the distribution π can be obtained as follows

$$\mathcal{R}\pi(t, \boldsymbol{\theta}) = \int \pi(\mathbf{x}) \delta(t - \mathbf{x}^\top \boldsymbol{\theta}) d\mathbf{x}, \quad \forall t \in \mathbb{R}. \quad (25)$$

¹We use a single multi layer perceptron (MLP) layer with normalized output as the h function.

Because, in practice, only samples from the distributions are available we aim to calculate a Radon slice of the empirical distribution of M samples $\pi_M = \frac{1}{M} \sum_{m=1}^M \delta(\mathbf{x} - \mathbf{x}_m)$:

$$\mathcal{R}\pi(t, \boldsymbol{\theta}) \approx \frac{1}{M} \sum_{m=1}^M \int \delta(\mathbf{x} - \mathbf{x}_m) \delta(t - \mathbf{x}^\top \boldsymbol{\theta}) d\mathbf{x} \quad (26)$$

$$= \frac{1}{M} \sum_{m=1}^M \delta(t - \mathbf{x}_m^\top \boldsymbol{\theta}). \quad (27)$$

By using the approximation in Eq. 27 and the empirical implementation of 1D Wasserstein distance (Eq. 24), we are able to compute a proxy to the original distance in Eq. 16.

C Pseudocode of Prior Optimization Procedure

Algorithm 1 describes the procedure of prior optimization for BAES.

Algorithm 1: Prior Optimization

Input: Empirical distribution $\tilde{\pi}(\mathbf{x})$; prior over parameters $p_\psi(\mathbf{w})$; number of prior samples N_S ; mini-batch size N_B ; number of random projections K ; regularization coefficient λ_C .

Output: The optimized prior's parameters ψ

```

1 while  $\psi$  has not converged do
2   Sample  $\mathbf{x} = \{\mathbf{x}_i\}_{i=1}^{N_B}$  from  $\tilde{\pi}(\mathbf{x})$  // Sample input data
3   Sample  $\mathcal{W} = \{\mathbf{w}_i\}_{i=1}^{N_S}$  from  $p_\psi(\mathbf{w})$  // Sample parameters from the prior
4   foreach  $\mathbf{w}_i \in \mathcal{W}$  do
5     /* Following steps are performed in a batch manner */
6      $\hat{\mathbf{x}}_i = (f_{\text{dec}} \circ f_{\text{enc}})(\mathbf{x})$  // Compute the functional outputs from Autoencoder
7     Sample  $\tilde{\mathbf{x}}_i$  from  $p(\mathbf{x} | \hat{\mathbf{x}}_i)$  // Sample from the likelihood
8   Gather samples  $\tilde{\mathbf{x}} = \cup \{\tilde{\mathbf{x}}_i\}_{i=1}^{N_S}$ 
9    $\mathcal{L} = DSW_2(\mathbf{x}, \tilde{\mathbf{x}}; K, \lambda_C)$  // Compute the  $DSW_2$  distance using Eq. 18
10   $\psi \leftarrow \text{Optimizer}(\psi, \nabla_\psi \mathcal{L})$  // Update prior's parameters

```

D Details on Stochastic gradient Hamiltonian Monte Carlo

Hamiltonian Monte Carlo (HMC) [49] is a highly-efficient Markov Chain Monte Carlo (MCMC) method used to generate samples from the posterior $\mathbf{w} \sim p(\mathbf{w} | \mathbf{x})$. HMC considers the joint log-likelihood as a potential energy function $U(\mathbf{w}) = -\log p(\mathbf{x} | \mathbf{w}) - \log p(\mathbf{w})$, and introduces a set of auxiliary momentum variable \mathbf{r} . Samples are generated from the joint distribution $p(\mathbf{w}, \mathbf{r})$ based on the Hamiltonian dynamics:

$$\begin{cases} d\mathbf{w} &= \mathbf{M}^{-1} \mathbf{r} dt, \\ d\mathbf{r} &= -\nabla U(\mathbf{w}) dt, \end{cases} \quad (28)$$

where, \mathbf{M} is an arbitrary mass matrix that plays the role of a preconditioner. In practice, this continuous system is approximated by means of ε -discretized numerical integration, and followed by Metropolis steps to accommodate numerical errors stemming from the integration.

However, HMC is not practical for large datasets due to the cost of computing the gradient $\nabla U(\mathbf{w}) = \nabla \log(\mathbf{x} | \mathbf{w})$ on the entire dataset. To mitigate this issue, [11] proposed SGHMC, which uses a noisy, unbiased estimate of the gradient $\nabla \tilde{U}(\mathbf{w})$ which is computed from a mini-batch of the data. The discretized Hamiltonian dynamics are then updated as follows

$$\begin{cases} \Delta \mathbf{w} &= \varepsilon \mathbf{M}^{-1} \mathbf{r}, \\ \Delta \mathbf{r} &= -\varepsilon \nabla \tilde{U}(\mathbf{w}) - \varepsilon \mathbf{C} \mathbf{M}^{-1} \mathbf{r} + \mathcal{N}(0, 2\varepsilon(\mathbf{C} - \tilde{\mathbf{B}})), \end{cases} \quad (29)$$

where ε is an step size, \mathbf{C} is an user-defined friction matrix, $\tilde{\mathbf{B}}$ is the estimate for the noise of the gradient evaluation. To choose these hyper-parameters, we use a scale-adapted version of SGHMC [56], where the hyper-parameters are adjusted automatically during a burn-in phase. After this period, all hyperparameters stay fixed.

Estimating M. We set the mass matrix $\mathbf{M}^{-1} = \text{diag}(\hat{V}_{\mathbf{w}}^{-1/2})$, where $\hat{V}_{\mathbf{w}}^{-1/2}$ is an estimate of the uncentered variance of the gradient, $\hat{V}_{\mathbf{w}}^{-1/2} \approx \mathbb{E}[(\nabla \tilde{U}(\mathbf{w}))^2]$, which can be estimated by using exponential moving average as follows

$$\Delta \hat{V}_{\mathbf{w}} = -\tau^{-1} \hat{V}_{\mathbf{w}} + \tau^{-1} \nabla(\tilde{U}(\mathbf{w}))^2, \quad (30)$$

where τ is a parameter vector that specifies the moving average windows. This parameter can be automatically chosen by using an adaptive estimate [56] as follows

$$\Delta \tau = -g_{\mathbf{w}}^2 \hat{V}_{\mathbf{w}}^{-1} \tau + 1, \quad \text{and}, \quad \Delta g_{\mathbf{w}} = -\tau^{-1} g_{\mathbf{w}} + \tau^{-1} \nabla \tilde{U}(\mathbf{w}), \quad (31)$$

where $g_{\mathbf{w}}$ is a smoothed estimate of the gradient $\nabla U(\mathbf{w})$.

Estimating $\tilde{\mathbf{B}}$. The estimate for the noise of the gradient evaluation, $\tilde{\mathbf{B}}$ should be ideally the estimate of empirical Fisher information matrix of $U(\mathbf{w})$, which is prohibitively expensive to compute. Therefore, we use a diagonal approximation, $\tilde{\mathbf{B}} = \frac{1}{2} \varepsilon \hat{V}_{\mathbf{w}}$, which is already available from the step of estimating M.

Choosing C. In practice, one can simply set the friction matrix as $\mathbf{C} = C\mathbf{I}$, i.e. the same independent noise for each elements of \mathbf{w} .

The discretized Hamiltonian dynamics. By substituting $\mathbf{v} := \varepsilon \hat{V}_{\mathbf{w}}^{-1/2} \mathbf{r}$, the dynamics Eq. 29 become

$$\begin{cases} \Delta \mathbf{w} &= \mathbf{v}, \\ \Delta \mathbf{v} &= -\varepsilon^2 \hat{V}_{\mathbf{w}}^{-1/2} \nabla \tilde{U}(\mathbf{w}) - \varepsilon C \hat{V}_{\mathbf{w}}^{-1/2} \mathbf{v} + \mathcal{N}(0, 2\varepsilon^3 C \hat{V}_{\mathbf{w}}^{-1} - \varepsilon^4 \mathbf{I}). \end{cases} \quad (32)$$

Following [56], we choose C such that $\varepsilon C \hat{V}_{\mathbf{w}}^{-1/2} = \alpha \mathbf{I}$. This is equivalent to using a constant momentum coefficient of α . The final discretized dynamics are then

$$\begin{cases} \Delta \mathbf{w} &= \mathbf{v}, \\ \Delta \mathbf{v} &= -\varepsilon^2 \hat{V}_{\mathbf{w}}^{-1/2} \nabla \tilde{U}(\mathbf{w}) - \alpha \mathbf{v} + \mathcal{N}(0, 2\varepsilon^2 \alpha \hat{V}_{\mathbf{w}}^{-1/2} - \varepsilon^4 \mathbf{I}). \end{cases} \quad (33)$$

E PCA of the SGD Trajectory

Inspired by [28], we use the subspace spanned by the SGD trajectory to visualize neural network's parameters in a low-dimensional space. This subspace is cheap to construct and can capture many of the sharp directions of the loss surface [28, 37, 44]. More specifically, we perform SGD starting from a MAP solution with a constant learning rate. Here, the loss function is the negative log joint likelihood of the BAE:

$$\mathcal{L}(\mathbf{w}) = -\frac{N}{M} \sum_{i=1}^M \log p(\mathbf{x}_i | \mathbf{w}) - \log p(\mathbf{w}), \quad (34)$$

where M is the mini-batch size and N is the size of training data. We store the deviations $\mathbf{a}_i = \bar{\mathbf{w}} - \mathbf{w}_i$ for the last M epochs, where $\bar{\mathbf{w}}$ is the running average of the first moment, M is determined by the amount of memory we can use. Then we perform PCA based on randomized SVD [23] on the matrix \mathbf{A} comprised of vectors $\mathbf{a}_1, \dots, \mathbf{a}_M$ to construct the subspace. The procedure is summarized in Algorithm 2.

Algorithm 2: Subspace construction with PCA

Input: Pretrained parameters \mathbf{w}_{MAP} ; learning rate η ; number of steps τ ; momentum update frequency c ; maximum number of columns M in deviation matrix \mathbf{A} .

Output: Shift vector $\bar{\mathbf{w}}$; projection matrix \mathbf{P} for subspace.

```
1  $\bar{\mathbf{w}} \leftarrow \mathbf{w}_{\text{MAP}}$  // Initialize mean
2 for  $i \leftarrow 1, 2, \dots, T$  do
3    $\mathbf{w}_i \leftarrow \mathbf{w}_{i-1} - \eta \nabla_{\mathbf{w}} \mathcal{L}(\mathbf{w}_{i-1})$  // Perform SGD update
4   if  $\text{MOD}(i, c) = 0$  then
5      $n \leftarrow i/c$  // Number of models
6      $\bar{\mathbf{w}} \leftarrow \frac{n\bar{\mathbf{w}} + \mathbf{w}_i}{n+1}$  // Update mean
7     if  $\text{NUM\_COLS}(\mathbf{A}) = M$  then
8       REMOVE_COL( $\mathbf{A}[:, 1]$ )
9       APPEND_COL( $\mathbf{A}, \mathbf{w}_i - \bar{\mathbf{w}}$ ) // Store deviation
10  $\mathbf{U}, \mathbf{S}, \mathbf{V}^\top \leftarrow \text{SVD}(\mathbf{A})$  // Perform truncated SVD
11 Return:  $\bar{\mathbf{w}}, \mathbf{P} = \mathbf{S}\mathbf{V}^\top$ 
```

F Additional Details on Experimental Settings

F.1 Experimental environment

In our experiments, we use 4 workstations, which have the following specifications:

- **GPU:** NVIDIA Tesla P100 PCIe 16 GB.
- **CPU:** Intel(R) Xeon(R) (4 cores) @ 2.30GHz.
- **Memory:** 25.5 GiB (DDR3).

F.2 Preprocessing data

- MNIST [36]: The dataset is publicly available at <http://yann.lecun.com/exdb/mnist>. We keep the original resolution of $1 \times 28 \times 28$ of the MNIST dataset.
- FREY-YALE [15]: The FREY and YALE datasets are publicly available at <http://cs.nyu.edu/~roweis/data.html> and <http://vision.ucsd.edu/extyaleb/CroppedYaleBZip>, respectively. All the images of FREY and YALE datasets are resized to the $1 \times 28 \times 28$ resolution.
- CELEBA [38]: The dataset is publicly available at <http://mmlab.ie.cuhk.edu.hk/projects/CelebA.html>. According to [17], we pre-process CELEBA images by first taking a 148×148 center crop and then resizing to the $3 \times 64 \times 64$ resolution.

F.3 Network architectures

In our experiments, we use convolutional networks for modeling both encoders and decoders. For a fair comparison, we employ the same network architecture for all models. The network’s parameters are initialized by using the default scheme in PyTorch [53].

Table 1 shows details on the network architectures used in our experimental campaign.

	MNIST	FREY-YALE	CELEBA
ENCODER:	$x \in \mathbb{R}^{1 \times 28 \times 28}$	$x \in \mathbb{R}^{1 \times 28 \times 28}$	$x \in \mathbb{R}^{3 \times 64 \times 64}$
	→ CONV ₃₂ → LEAKY RELU	→ CONV ₆₄ → LEAKY RELU	→ CONV ₆₄ → LEAKY RELU
	→ CONV ₆₄ → LEAKY RELU	→ CONV ₁₂₈ → LEAKY RELU	→ CONV ₁₂₈ → LEAKY RELU
	→ CONV ₆₄ → LEAKY RELU	→ CONV ₁₂₈ → LEAKY RELU	→ CONV ₂₅₆ → LEAKY RELU
	→ CONV ₁₂₈ → LEAKY RELU	→ CONV ₂₅₆ → LEAKY RELU	→ CONV ₅₁₂ → LEAKY RELU
	→ FLATTEN → FC _{50×M}	→ FLATTEN → FC _{50×M}	→ FLATTEN → FC _{50×M}
DECODER:	$z \in \mathbb{R}^{50} \rightarrow$ FC _{7×7×128}	$z \in \mathbb{R}^{50} \rightarrow$ FC _{7×7×256}	$z \in \mathbb{R}^{50} \rightarrow$ FC _{8×8×512}
	→ LEAKY RELU	→ LEAKY RELU	→ LEAKY RELU
	→ CONV _{T128} → LEAKY RELU	→ CONV _{T256} → LEAKY RELU	→ CONV _{T512} → LEAKY RELU
	→ CONV _{T64} → LEAKY RELU	→ CONV _{T128} → LEAKY RELU	→ CONV _{T256} → LEAKY RELU
	→ CONV _{T64} → LEAKY RELU	→ CONV _{T128} → LEAKY RELU	→ CONV _{T128} → LEAKY RELU
	→ CONV _{T1} → SIGMOID	→ CONV _{T1} → SIGMOID	→ CONV _{T1} → SIGMOID

Table 1: Convolutional Encoder-Decoder architectures. CONV_n denotes a convolutional layer with n filters, whereas FC_n represents a fully-connected layer with n units. All convolutions CONV_n and transposed convolutions CONV_T_n have a filter size of 4×4 for MNIST and FREY-YALE and 5×5 for CELEBA. $M = 1$ for all models except for the VAES which have $M = 2$ as the encoder has to yield both mean and variance for each input.

F.4 Prior optimization

As done in [50], we use a single-layer multilayer perceptron (MLP), h_ϕ , to represent the Borel measurable function in the dual form of DSWD (Eq. 18). At each iteration of Algorithm 1, to find a local maxima, we optimize h_ϕ for 30 epochs by using an Adam optimizer [31] with a learning rate of 0.0005. We use another Adam optimizer with a learning rate of 0.001 to update the prior’s parameters. We use a mini-batch size of $N_B = 64$ and then generate $N_s = 32$ prior samples given each data point. By default, we use $K = 1000$ random projections with a regularization coefficient $\lambda_C = 100$ to estimate the 2-Wasserstein distance. The convergences of prior optimization on MNIST, FREY and CELEBA datasets are illustrated in Fig. 16.

F.5 SGHMC hyper-parameters

In Table 2 we report the hyper-parameters used in the experiments on MNIST, YALE and CELEBA datasets. As seen, we always use a fixed step size of 0.003, a momentum coefficient of 0.05, and a mini-batch size of 64. The number of collected samples after thinning is 32. The number of burn-in iterations and the thinning interval are increased according to the size of the training set.

TRAINING SIZE	MNIST				YALE				CELEBA			
	200	500	1000	2000	50	100	200	500	500	1000	2000	4000
MINI-BATCH SIZE	64	64	64	64	64	64	64	64	64	64	64	64
STEP SIZE (10^{-3})	3	3	3	3	3	3	3	3	3	3	3	3
MOMENTUM (10^{-2})	5	5	5	5	5	5	5	5	5	5	5	5
NUM. BURN-IN STEPS (10^3)	6	6	6	6	6	6	6	6	6	20	20	20
NUM. SAMPLES	32	32	32	32	32	32	32	32	32	32	32	32
THINNING INTERVAL (10^3)	1	1	1	2	1	1	1	1	1	2	3	5

Table 2: SGHMC hyper-parameters used in the experiments on MNIST, YALE and CELEBA datasets.

F.6 Competing approaches

- **VAE [32]:** The vanilla VAE model employed with a Gaussian encoder and a standard Gaussian prior on the latent space.
- **β -VAE [26]:** The KL term in the VAE’s objective is weighted by $\beta = 0.1$ to reduce the effect of the prior. This helps to avoid the over-regularization problem of VAES and improve reconstruction quality.
- **VAE + Sylvester Flows [61]:** One of the state-of-the-art normalizing flows for the encoder of VAES, which has richer expressiveness than VAE’s post-Gaussian encoder. As employed in [61], we use Orthogonal Sylvester flows with 4 transformations and 32 orthogonal vectors.

- **VAE + VampPrior** [59]: A flexible prior for VAEs, which is a mixture of variational posteriors conditioned on learnable pseudo-observations. This allows the variational posterior to learn more a potential latent representation. Due to using small training data, we use 100 trainable pseudo-observations in our experiments. We found that increasing more pseudo-observations may hurt the predictive performance because of overfitting.
- **2-Stage VAE** [14]: A simple and practical method to improve the quality of generated images from VAEs by performing a form of ex-post density estimation via a second VAE. As employed in [14], for the second-stage VAE, we use a MLP having three 1024-dimensional hidden layers with ReLU activation function.
- **WAE** [58] Wasserstein Autoencoder: This model is an alternative of VAEs. By reformulating the objective function as an OT problem, WAE regularizes the averaged encoding distribution instead of each data point. This encourages the encoded training distribution to match the prior while still allowing to learn significant information from the data. As suggested in [58], we use WAE-MMD with the inverse multiquadratics kernel and a regularization coefficient $\lambda = 10$ due to its stability compared to WAE-GAN. We impose the standard Gaussian prior on the latent space.
- **NS-GAN** [21]: a standard GAN with the non-saturating loss, which has been shown to be robust to the choice of hyper-parameters on CELEBA [40]. For a fair comparison, we reuse the encoder and decoder architectures for the discriminator and generator, respectively.
- **DiffAugment-GAN** [69]: a more complex architecture [STYLEGAN2, see 30] combined with a powerful differentiable augmentation scheme, specifically developed for low data regimes. We refer to the original work of [69] and the implementation in <https://github.com/mit-han-lab/data-efficient-gans> for additional details on the network architecture. We use the same latent size of 50, a maximum of 64 feature maps, and all available augmentations (color, cutout and translation). The remaining parameters are left at default value.

All autoencoder models are trained for 200 epochs with an Adam optimizer [31] using the default hyper-parameters in PyTorch, i.e. learning rate = 0.001, $\beta_1 = 0.9$, $\beta_2 = 0.999$. The NS-GAN is trained for 200 epochs with a learning rate of 0.0002. The DiffAugment-GAN is trained with learning rate of 0.001 for 1 million steps (except for the case of 4 000 training samples, which was extended for 2 millions steps).

F.7 Performance evaluation

Test log-likelihood. To evaluate the reconstruction quality, we use the mean predictive log-likelihood evaluated over the test set. This metric tells us how probable it is that the test targets were generated using the test inputs and our model. Notice that for the case of autoencoder models, the test targets are exactly the test inputs. The predictive likelihood is a proper scoring rule [20] that depends on both the accuracy of predictions and their uncertainty.

For BAE, as done in the literature of BNNs [29, 52], we can estimate the predictive likelihood for an unseen datapoint, \mathbf{x}^* , as follows

$$\mathbb{E}_{p(\mathbf{w}|\mathbf{x})}[p(\mathbf{x}^*|\mathbf{w})] \approx \frac{1}{M} \sum_{i=1}^M p(\mathbf{x}^*|\mathbf{w}_i), \quad \mathbf{w}_i \sim p(\mathbf{w}|\mathbf{x}),$$

where \mathbf{w}_i is a sample from the posterior $p(\mathbf{w}|\mathbf{x})$ obtained from the SGHMC sampler.

For VAEs, because the randomness comes from the latent code not the network’s parameters, we can use MC approximation to estimate the predictive likelihood as follows

$$\mathbb{E}_{q(\mathbf{z}|\mathbf{x}^*)}[p(\mathbf{x}^*|\mathbf{z})] \approx \frac{1}{N} \sum_{i=1}^N p(\mathbf{x}^*|\mathbf{z}_i), \quad \mathbf{z}_i \sim q(\mathbf{z}|\mathbf{x}^*),$$

where $q(\mathbf{z}|\mathbf{x}^*)$ is the amortized approximate posterior. In our experiments, we use $N = 200$.

For completeness, we also report the test marginal log-likelihood $p(\mathbf{x})$ of VAEs, which is estimated by the importance weighted sampling (IWAE) method [10]. More specifically,

$$\text{IWAE} = \log \left(\frac{1}{K} \sum_{i=1}^K \frac{p(\mathbf{x}^*, \mathbf{z}_i)}{q(\mathbf{z}_i | \mathbf{x}^*)} \right), \quad \mathbf{z}_i \sim q(\mathbf{z} | \mathbf{x}^*).$$

It can be shown that IWAE lower bounds $\log p(\mathbf{x}^*)$ and can be arbitrarily close to the target as the number of samples K grows. We use $K = 1000$ in the experiments. The full results of test marginal log-likelihood are reported in Tables 7, 8 and 9.

FID score. To assess the quality of the generated images, we employed the widely used Fréchet Inception Distance [25]. This metric is the Fréchet distance between two multivariate Gaussians, the generated samples and real data samples are compared through their distribution statistics:

$$\text{FID} = \|\mu_{\text{real}} - \mu_{\text{gen}}\|^2 + \text{Tr}(\Sigma_{\text{real}} + \Sigma_{\text{gen}} - 2\sqrt{\Sigma_{\text{real}}\Sigma_{\text{gen}}}). \quad (35)$$

Two distribution samples are calculated from the 2048-dimensional activations of pool3 layer of Inception-v3 network². In our experiments, the statistics of generated and real data are computed over 10000 generated images and test data, respectively.

²We use the original TensorFlow implementation of FID score which is available at <https://github.com/bioinf-jku/TTUR>.

G Additional Results of Comparison with Temperature Scaling

In Bayesian deep learning, *temperature scaling* is a practical technique to improve predictive performance [28, 63, 67]. There are two main approaches to tempering the posterior, namely (1) *partial tempering* and (2) *full tempering* [1, 66]. In this section, we investigate rigorously the posteriors induced by the $\mathcal{N}(0, 1)$ prior and optimized prior under different tempering settings. We use the same setup of MNIST as in the main paper, with 200 examples for inference. For the optimized prior, we use 100 training samples for learning prior. For the $\mathcal{N}(0, 1)$ prior, we use the union of 200 training samples and the data used to optimized prior for training.

G.1 Partial Tempering

The *partially tempered* posterior is defined as follows [28, 64]

$$p_{\tau_{\text{partial}}}(\mathbf{w} | \mathbf{x}) \propto \underbrace{p(\mathbf{x} | \mathbf{w})}_{\text{likelihood}}^{1/\tau} \underbrace{p(\mathbf{w})}_{\text{prior}},$$

where $\tau > 0$ is a *temperature* value. This parameter controls how the prior and likelihood interact in the posterior. When $\tau = 1$ the true posterior is recovered, and as τ becomes large, the tempered posterior approaches the prior. In the case of small training data and using a misspecified prior such as $\mathcal{N}(0, 1)$, we would use a small temperature value (e.g. $\tau < 1$) to *reduce the effect of the prior*. This corresponds to artificially sharpening the posterior by overcounting the data by a factor of τ .

Fig. 9a shows the test LL on MNIST for BAE with $\mathcal{N}(0, 1)$ prior and different temperature values. As expected, the predictive performance of the posterior obtained via low temperatures $\tau < 1$ is much better than those at high temperatures $\tau > 1$. However, cooling the posterior only shows slight improvement compared to the true posterior induced from the optimized prior. In addition, in case $\tau > 1$, where the influence of the posterior becomes stronger, the tempered posterior w.r.t. the optimized prior is significantly better than using the $\mathcal{N}(0, 1)$ prior. This again shows clearly that $\mathcal{N}(0, 1)$ is a poor prior for a deep BAE.

Fig. 10a illustrates samples from priors and posteriors in a low-dimensional space. We also consider the posterior obtained from the *entire* training data and the $\mathcal{N}(0, 1)$ prior as “oracle” posterior. In this case, the choice of the prior does not strongly affect the posterior as this is dominated by the likelihood. It can be seen that, for high-temperature values $\tau > 1$, the *warm posteriors* w.r.t. $\mathcal{N}(0, 1)$ prior are stretched out as the prior effect is too strong. These posteriors are mismatched with the “oracle” posterior as further confirmed by very low test log-likelihood. Meanwhile, due to the good inductive bias from the optimized prior, the corresponding tempered posterior is still located in regions nearby the “oracle” posterior. For low temperature values $\tau < 1$, the *cold posteriors* are more concentrated by overcounting evidence. However, if we use a very small temperature (e.g. $\tau = 10^{-5}$), the resulting posterior overly concentrates around the MLE, becoming too constrained by the training data.

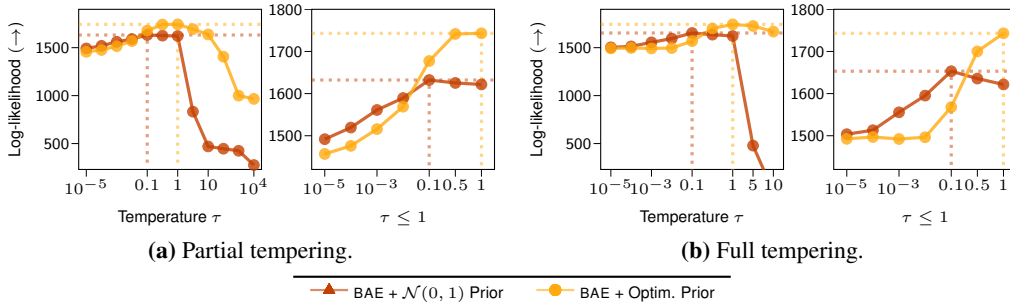


Figure 9: Test LL as a function of temperature on MNIST using BAE with $\mathcal{N}(0, 1)$ prior. The dotted lines indicate the best performance of LL.

G.2 Full Tempering

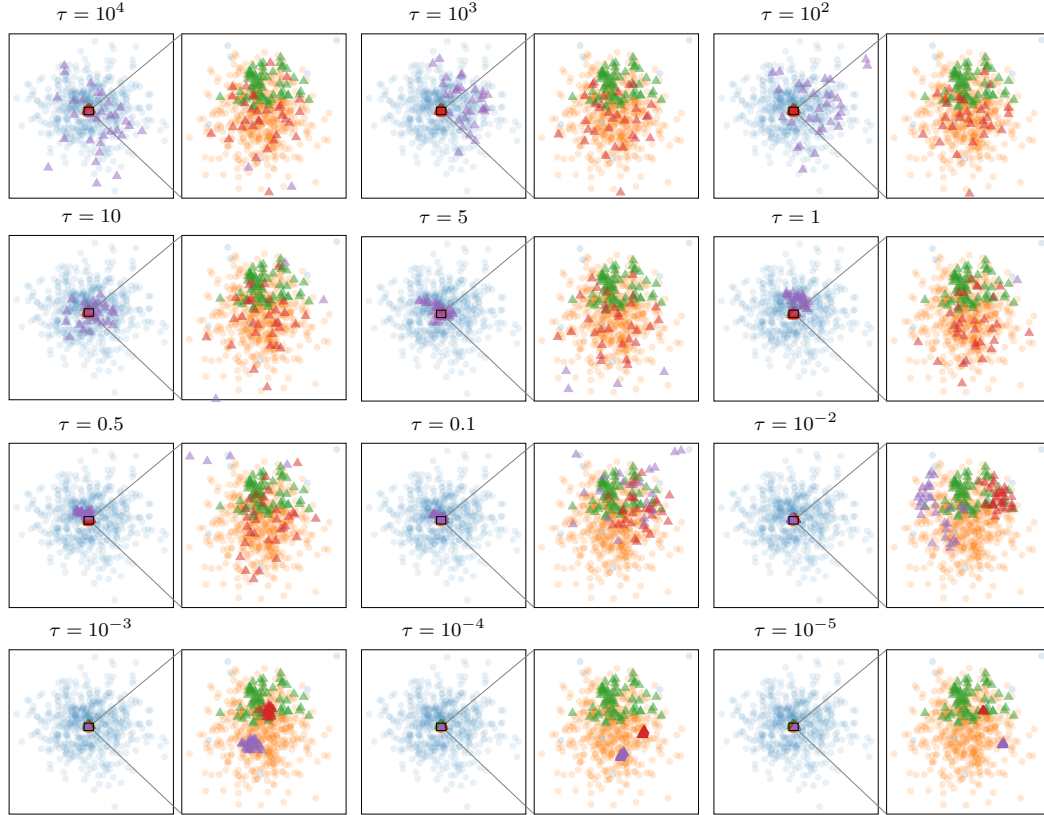
For the fully tempered posterior, instead of scaling the likelihood term only, we scale the whole posterior as follows

$$p_{\tau_{\text{full}}}(\mathbf{w} | \mathbf{x}) \propto \underbrace{(p(\mathbf{x} | \mathbf{w}))}_{\text{likelihood}} \underbrace{p(\mathbf{w})}_{\text{prior}})^{1/\tau}.$$

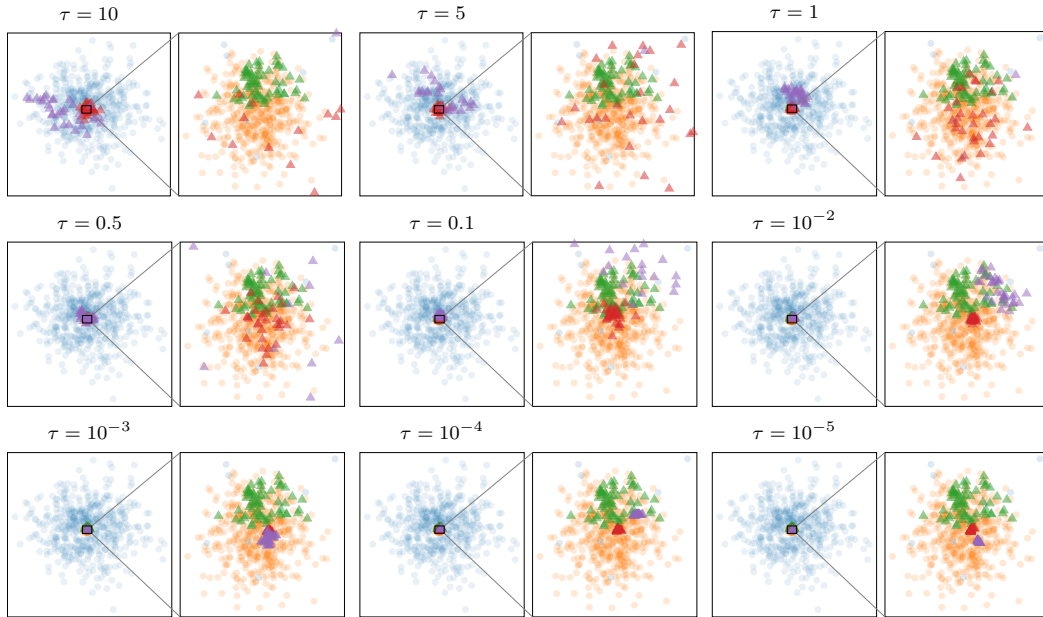
The only difference between partial and full tempering is whether we scale the prior. If we place Gaussian priors on the parameters, this scaling can be absorbed into the prior variance, $\sigma_{\text{full}}^2 = \sigma_{\text{partial}}^2 / \tau$.

Recently, [63] argues that BNNs require a cold posterior, where a $\tau < 1$ is employed, to obtain a good performance. However, we hypothesize that *the cold posterior effect* may originate from using a poor prior. In this case, as shown in Fig. 9b, the results of full tempering are similar to those of partial tempering. Cooling the posterior only helps to increase slightly predictive performance for $\mathcal{N}(0, 1)$ prior. We also observe that the MCMC sampling is not converged if a very large τ is employed, thus we only consider small values of τ (e.g. $\tau \in \{5, 10\}$). In these cases, as depicted in Fig. 10b, the samples from the posterior may be outside of the hypothesis space of the optimized prior.

In sum, the true posterior induced from our optimized prior is remarkably better than any types of tempered posteriors. These results suggest that, in the small-data regime, we should choose carefully a more sensible prior rather than simply using a vague prior and overcounting the data.



(a) Partial tempering.



(b) Full tempering.

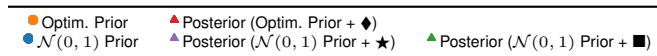


Figure 10: Visualization of samples from priors and posteriors of BAE’s parameters in the plane spanned by eigenvectors of the SGD trajectory. ◆ indicates using 200 samples for training; ★ indicates using the union of these samples and 100 samples used for learning the prior; ■ denotes using all 60000 training samples. Here, τ is the temperature value used for the ◆ and ★ cases. All plots are produced using convolutional BAE on MNIST.

H Ablation Studies

H.1 Additional results of ablation study on the size of the dataset to optimize priors

In this experiment, we demonstrate that we can obtain a sensible result by using a small number of training instances to optimize the prior. Here, we use a set of 200 samples of 0-9 digits for inference, and another dataset also consisting of 0-9 digits for optimizing the prior. Fig. 13 shows the predictive performance and samples from the posterior. We observe that the performance gain by using more data is not significant. We can achieve sensible results by using only about 10-50 samples for each class. In addition, as illustrated in the low-dimensional space (Fig. 13), the hypothesis space of the prior is not collapsed as we increase the size of the dataset used to optimize the prior. As a result, the predictive posterior is also not concentrated to the MLE solutions as further demonstrated in Fig. 12. This behavior is very different from overcounting the data by using temperature scaling, where the posterior becomes more concentrated as the temperature is decreased. This again demonstrates the practicality of our proposed method in the small-data regime.

H.2 Effect of the dimensionality of latent space

Fig. 11 illustrates the predictive performance of VAEs and BAEs in terms test LL on MNIST for different size of the latent space and training size. It is clear that BAEs with optimized prior consistently outperforms other competitors across all dimensionalities of the latent space and training sizes.

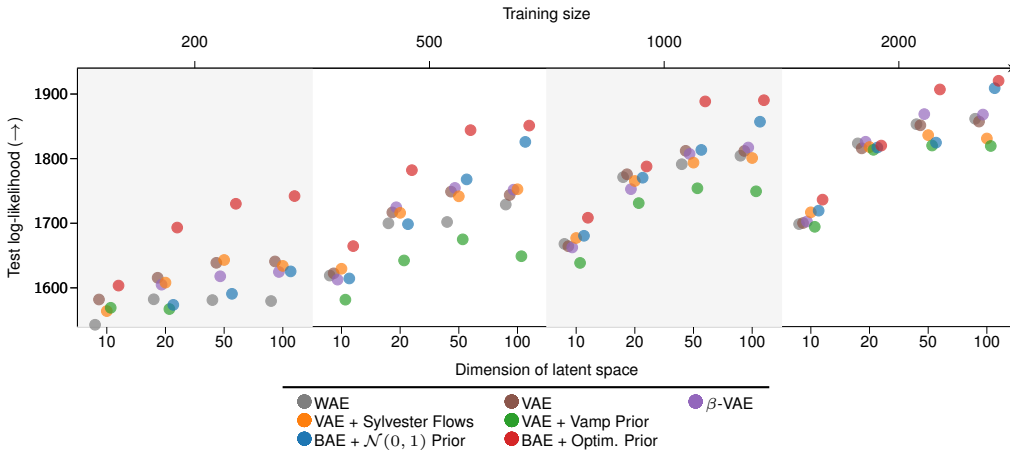


Figure 11: Ablation study on the test LL on MNIST dataset for different sizes of the latent space and training sizes.

H.3 Visualizing 2-dimensional latent space

We run several experiments with a low latent space ($K = 2$) to test the efficacy of VAEs and BAEs as dimensionality reduction techniques. Fig. 14 shows the results, where each color represents an MNIST digit. As seen, BAE with optimized prior produces a more well-defined class structure in comparison with other methods.

We also consider the 2D latent space to visualize that ex-post density estimation with DPMM helps to reduce the mismatch between the aggregated posterior and the prior. As can be seen from Fig. 15, there are large mismatches between aggregated posterior of VAEs and the $\mathcal{N}(0, 1)$ prior. We can reduce this problem by using a more expressive prior like VampPrior, or performing ex-post density estimation with a second VAE. For BAEs, it is clear that the flexible DPMM estimator effectively fixes the mismatch and this results in better sample quality as reported in the main paper.

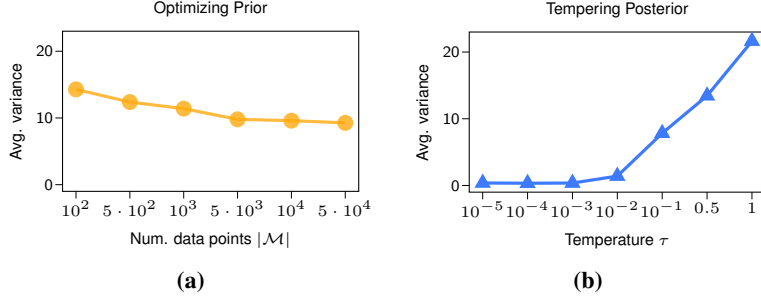


Figure 12: The average predictive variance computed over test datapoints as a function of (a) the number of data points used to optimize prior, and (b) the temperature used for cooling the posterior. Here, we use 200 datapoints from MNIST dataset for inference. In figure (a), we use the optimized prior and consider the true posterior without any tempering. In figure (b), we use the standard Gaussian prior and employ partial tempering for the posterior.

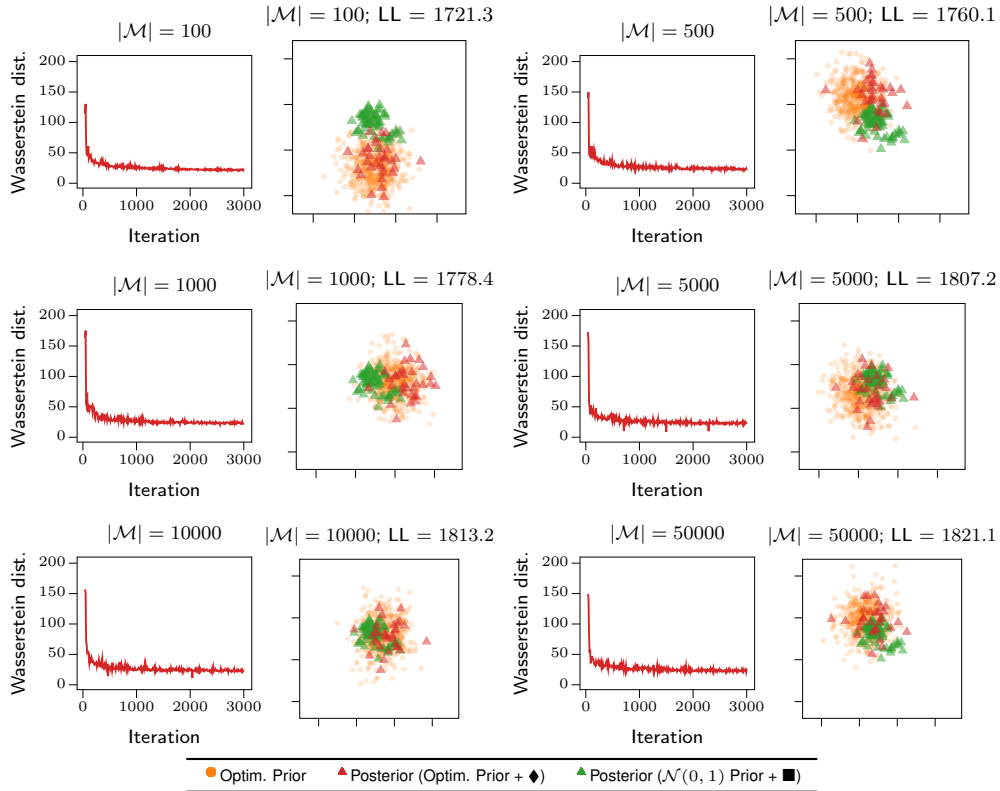


Figure 13: Visualization of convergence Wasserstein optimization, and samples from priors and posteriors of BAE’s parameters in the plane spanned by eigenvectors of the SGD trajectory corresponding to the first and second largest eigenvalues. Here, $|\mathcal{M}|$ is the size of dataset used for optimizing the prior; \blacklozenge indicates using 200 training samples for inference; \blacksquare denotes using all 60000 training samples for inference; LL denotes the test log-likelihood performance of the posterior w.r.t. the optimized prior. All plots are produced using convolutional BAE on MNIST.

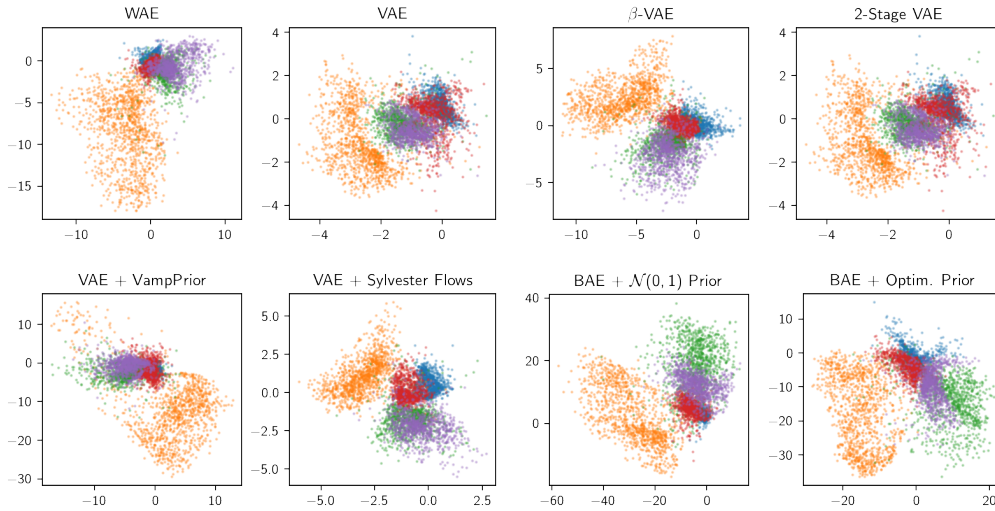


Figure 14: Visualization of 2D latent spaces of variants of autoencoders on MNIST test set where each color represents a digit class. We consider only 5 classes for easier visualization and comparison. All models are trained on 1000 training samples from MNIST dataset.

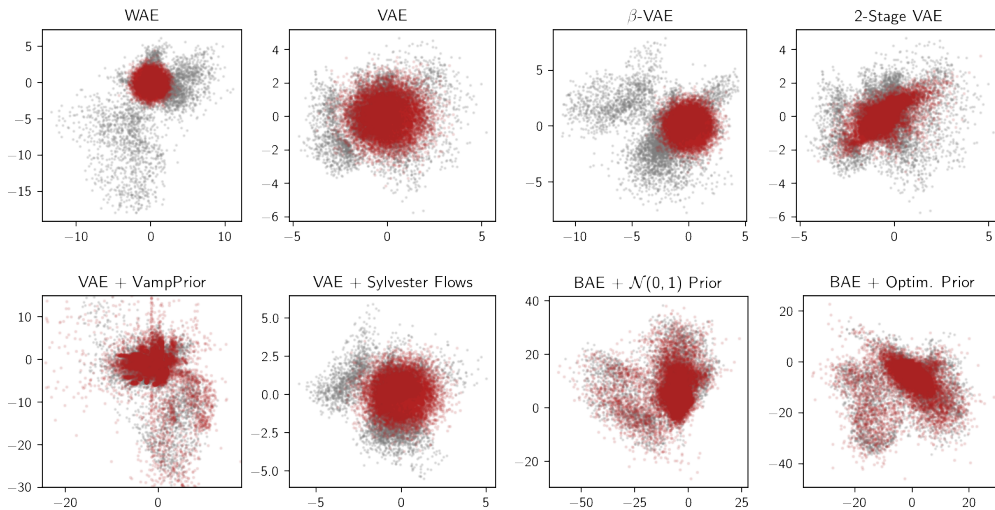


Figure 15: Different priors and density estimations on the 2-dimensional latent space of VAEs and BAEs. All models are trained on 1000 training samples from MNIST dataset. The gray points are test set samples while the red ones are samples from priors / density estimators. Here, we employ the isotropic Gaussian prior on the latent space of WAE, VAE, β -VAE and VAE with Sylvester Flows. The VampPrior is learned to explicitly model the aggregated posterior while 2-Stage VAE uses another VAE to estimate the density of the learned latent space. Meanwhile, for BAEs, we use DPMMs for ex-post density estimation.

I Additional Results

I.1 Convergence of Wasserstein optimization

Fig. 16 depicts the progressions of Wasserstein optimization in the MNIST, FREY-YALE and CELEBA experiments.

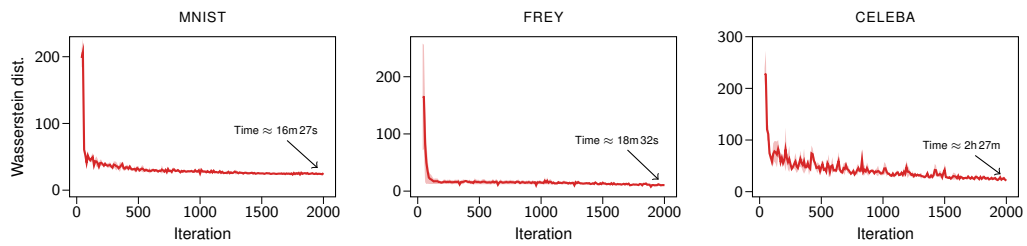


Figure 16: Convergence of Wasserstein optimization. The shaded areas represent the standard deviation computed over 4 random data splits.

I.2 Tabulated results

Detailed results on MNIST, YALE and CELEBA datasets are reported from Table 3 to Table 9.

TRAINING SIZE	LOG LIKELIHOOD (\uparrow)			
	200	500	1000	2000
WAE	1590.0 (11.0)	1732.7 (19.2)	1809.5 (11.1)	1857.4 (4.8)
★ WAE	1675.2 (10.6)	1779.6 (10.2)	1839.3 (6.1)	1871.1 (3.1)
VAE	1635.1 (8.0)	1744.6 (4.5)	1805.5 (4.8)	1847.1 (3.7)
★ VAE	1697.0 (9.9)	1776.2 (6.8)	1829.5 (2.8)	1849.9 (4.4)
β -VAE	1626.2 (10.3)	1749.7 (9.2)	1812.8 (3.8)	1862.3 (4.9)
★ β -VAE	1698.2 (8.0)	1780.2 (9.3)	1841.2 (3.4)	1871.9 (4.4)
VAE + SYLVESTER FLOWS	1635.4 (6.1)	1743.5 (1.5)	1799.1 (5.5)	1836.3 (7.2)
★ VAE + SYLVESTER FLOWS	1711.4 (3.0)	1781.0 (2.9)	1816.7 (6.2)	1848.1 (6.5)
VAE + VAMPRIOR	1543.0 (12.6)	1669.9 (22.0)	1756.8 (2.6)	1818.6 (3.6)
★ VAE + VAMPRIOR	1609.6 (14.4)	1732.1 (14.2)	1798.1 (5.4)	1839.3 (4.0)
BAE + $\mathcal{N}(0, 1)$ PRIOR	1609.0 (10.6)	1761.0 (9.1)	1837.6 (18.4)	1827.9 (5.7)
★ BAE + $\mathcal{N}(0, 1)$ PRIOR	1681.2 (24.5)	1798.6 (22.8)	1827.0 (35.9)	1842.2 (37.4)
BAE + OPTIM. PRIOR (OURS)	1743.5 (12.0)	1845.1 (1.2)	1879.1 (6.3)	1906.8 (1.1)

Table 3: Evaluation of all methods in terms of test log-likelihood (*the higher, the better*) on MNIST. The parentheses are the standard deviations. ★ indicates that we use the union of the training data and the data used to optimize prior to train the model.

TRAINING SIZE	LOG LIKELIHOOD (\uparrow)			
	50	100	200	500
WAE	689.7 (10.4)	724.8 (4.4)	754.5 (3.9)	787.0 (0.7)
★ WAE	718.4 (0.9)	740.6 (4.6)	765.7 (2.2)	794.3 (1.6)
VAE	692.3 (8.4)	723.5 (2.8)	738.4 (3.2)	774.1 (1.3)
★ VAE	701.2 (5.9)	728.2 (3.5)	749.4 (2.0)	774.8 (2.1)
β -VAE	707.1 (5.7)	733.8 (8.5)	761.1 (3.4)	791.8 (0.7)
★ β -VAE	712.1 (7.6)	737.8 (4.7)	763.4 (1.3)	790.8 (1.5)
VAE + SYLVESTER FLOWS	705.4 (4.8)	729.3 (4.4)	738.2 (1.6)	766.8 (0.9)
★ VAE + SYLVESTER FLOWS	682.1 (11.7)	716.3 (4.3)	739.6 (2.1)	765.3 (1.2)
VAE + VAMPRIOR	690.0 (6.9)	722.8 (1.9)	740.6 (1.8)	766.8 (2.7)
★ VAE + VAMPRIOR	691.7 (6.1)	716.9 (4.7)	737.8 (5.3)	764.2 (2.2)
BAE + $\mathcal{N}(0, 1)$ PRIOR	426.1 (27.6)	668.8 (12.8)	724.9 (21.2)	775.5 (4.6)
★ BAE + $\mathcal{N}(0, 1)$ PRIOR	388.0 (13.6)	570.4 (9.1)	688.2 (5.1)	752.5 (1.0)
BAE + OPTIM. PRIOR (OURS)	730.3 (3.0)	754.3 (3.1)	771.6 (3.0)	793.5 (2.0)

Table 4: Evaluation of all methods in terms of test log-likelihood (*the higher, the better*) on YALE. The same interpretation as Table 3.

TRAINING SIZE	LOG LIKELIHOOD (\uparrow)			
	500	1000	2000	4000
WAE	5732.6 (35.3)	6266.4 (73.4)	6703.6 (24.9)	6928.3 (32.5)
★ WAE	6509.7 (49.2)	6659.8 (30.4)	6864.0 (23.7)	7021.6 (24.3)
VAE	5914.2 (78.3)	6406.4 (39.6)	6683.6 (87.5)	6976.4 (11.9)
★ VAE	6460.1 (33.7)	6694.1 (63.1)	6831.8 (97.2)	7039.5 (36.5)
β -VAE	5710.2 (49.0)	6192.5 (91.9)	6640.6 (139.4)	7000.9 (7.9)
★ β -VAE	6445.3 (94.0)	6654.6 (44.5)	6859.0 (39.8)	7007.7 (86.3)
VAE + SYLVESTER FLOWS	5481.6 (108.4)	5984.2 (37.4)	6415.5 (33.5)	6699.9 (46.9)
★ VAE + SYLVESTER FLOWS	6241.3 (149.2)	6437.2 (58.2)	6519.9 (88.5)	6831.5 (121.2)
VAE + VAMPPRIOR	5776.6 (95.9)	6242.2 (92.2)	6691.5 (24.4)	6999.7 (15.9)
★ VAE + VAMPPRIOR	6531.7 (61.5)	6591.6 (97.4)	6868.3 (27.8)	6990.7 (37.3)
2-STAGE VAE	5914.2 (78.3)	6406.4 (39.6)	6683.6 (87.5)	6976.4 (11.9)
★ 2-STAGE VAE	6460.1 (33.7)	6694.1 (63.1)	6831.8 (97.2)	7039.5 (36.5)
BAE + $\mathcal{N}(0, 1)$ PRIOR	5581.9 (70.8)	6273.3 (54.2)	6848.3 (15.1)	7154.5 (15.6)
★ BAE + $\mathcal{N}(0, 1)$ PRIOR	6574.1 (46.6)	6826.5 (31.0)	7038.3 (17.8)	7223.1 (13.2)
BAE + OPTIM. PRIOR (OURS)	6781.3 (32.4)	7065.8 (15.0)	7244.7 (8.7)	7370.0 (13.2)

Table 5: Evaluation of all methods in terms of test log-likelihood (*the higher, the better*) on CELEBA. The same interpretation as Table 3.

TRAINING SIZE	FID (\downarrow)			
	500	1000	2000	4000
WAE	342.14 (19.02)	309.79 (12.58)	275.10 (8.71)	253.06 (5.52)
★ WAE	294.26 (8.41)	276.24 (10.49)	261.64 (6.08)	246.92 (3.28)
VAE	271.70 (5.12)	240.69 (3.44)	230.61 (7.05)	209.08 (6.28)
★ VAE	248.18 (12.20)	237.29 (12.48)	231.50 (14.17)	206.92 (9.91)
β -VAE	323.00 (10.88)	295.54 (12.45)	276.71 (15.61)	250.61 (5.30)
★ β -VAE	285.81 (5.58)	277.44 (12.97)	271.82 (6.69)	262.72 (17.92)
VAE + SYLVESTER FLOWS	221.71 (10.50)	214.94 (12.01)	207.86 (9.93)	198.94 (10.10)
★ VAE + SYLVESTER FLOWS	210.24 (3.48)	215.00 (5.79)	204.42 (11.86)	179.26 (49.53)
VAE + VAMPPRIOR	144.41 (16.61)	131.02 (2.22)	112.82 (4.05)	96.20 (2.79)
★ VAE + VAMPPRIOR	120.02 (8.62)	120.23 (7.16)	102.67 (7.61)	95.95 (4.86)
2-STAGE VAE	78.23 (2.56)	69.37 (2.39)	67.69 (1.55)	74.47 (4.52)
★ 2-STAGE VAE	72.21 (3.05)	69.25 (3.32)	72.64 (4.62)	84.95 (3.91)
NS-GAN	252.33 (27.03)	171.18 (15.51)	205.05 (97.46)	128.29 (3.81)
★ NS-GAN	151.28 (2.27)	150.74 (4.39)	137.64 (4.14)	139.43 (8.77)
★ DIFFAUGMENT-GAN	66.09 (0.27)	58.76 (0.17)	50.22 (2.62)	45.14 (0.13)
BAE + $\mathcal{N}(0, 1)$ PRIOR	89.36 (4.56)	81.31 (2.50)	72.50 (1.37)	71.85 (0.17)
★ BAE + $\mathcal{N}(0, 1)$ PRIOR	86.03 (3.53)	75.86 (0.45)	71.21 (1.41)	70.72 (0.39)
BAE + OPTIM. PRIOR (OURS)	68.59 (3.08)	66.11 (0.96)	68.34 (0.86)	67.18 (0.80)

Table 6: Evaluation of all methods in terms of FID (*the lower, the better*) on CELEBA. The same interpretation as Table 3.

TRAINING SIZE	LOG MARGINAL LIKELIHOOD (\uparrow)			
	200	500	1000	2000
VAE	1648.2 (10.1)	1744.0 (5.6)	1795.1 (2.6)	1829.7 (2.5)
★ VAE	1702.4 (8.9)	1771.0 (6.7)	1816.2 (4.6)	1832.2 (4.8)
β -VAE	1497.1 (12.5)	1625.9 (7.7)	1687.3 (3.8)	1734.4 (4.2)
★ β -VAE	1570.1 (7.8)	1655.7 (7.9)	1715.2 (2.9)	1747.1 (5.6)
VAE + SYLVESTER FLOWS	1627.0 (6.9)	1709.8 (1.8)	1755.4 (4.6)	1783.3 (5.5)
★ VAE + SYLVESTER FLOWS	1688.0 (3.2)	1741.8 (2.5)	1771.4 (3.2)	1794.8 (5.0)
VAE + VAMPRIOR	1545.6 (10.5)	1681.7 (20.2)	1758.4 (4.1)	1810.7 (2.2)
★ VAE + VAMPRIOR	1616.3 (15.3)	1737.5 (11.4)	1795.6 (4.8)	1829.1 (2.6)

Table 7: Evaluation of all methods in terms of test log marginal likelihood of VAE models (*the higher, the better*) on MNIST. The same interpretation as Table 3.

TRAINING SIZE	LOG MARGINAL LIKELIHOOD (\uparrow)			
	50	100	200	500
VAE	693.8 (7.8)	720.8 (3.4)	734.5 (2.8)	767.2 (0.6)
★ VAE	704.2 (5.6)	723.7 (3.1)	742.4 (1.9)	765.1 (1.2)
β -VAE	628.1 (2.7)	655.2 (9.9)	683.0 (3.9)	712.5 (1.6)
★ β -VAE	658.5 (13.4)	683.9 (5.4)	707.2 (2.7)	731.5 (2.3)
VAE + SYLVESTER FLOWS	668.6 (5.2)	686.5 (3.4)	695.1 (1.5)	718.0 (0.8)
★ VAE + SYLVESTER FLOWS	655.6 (4.9)	677.2 (3.8)	695.7 (0.7)	717.2 (0.7)
VAE + VAMPRIOR	672.7 (7.9)	697.4 (6.8)	733.4 (3.2)	759.0 (1.2)
★ VAE + VAMPRIOR	703.9 (4.2)	721.5 (4.0)	736.8 (4.1)	760.0 (2.2)

Table 8: Evaluation of all methods in terms of test log marginal likelihood (*the higher, the better*) of VAE models on YALE. The same interpretation as Table 3.

TRAINING SIZE	LOG MARGINAL LIKELIHOOD (\uparrow)			
	500	1000	2000	4000
VAE	5973.4 (66.7)	6416.6 (36.6)	6673.7 (82.6)	6943.4 (8.7)
★ VAE	6470.0 (30.7)	6676.7 (57.4)	6807.6 (89.3)	7001.2 (37.5)
β -VAE	5496.0 (52.9)	6007.8 (89.8)	6457.8 (147.2)	6820.1 (7.4)
★ β -VAE	6294.4 (98.1)	6472.2 (46.1)	6680.5 (42.8)	6844.6 (93.9)
VAE + SYLVESTER FLOWS	5545.8 (97.8)	5988.2 (40.9)	6387.9 (37.8)	6649.9 (47.1)
★ VAE + SYLVESTER FLOWS	6226.9 (140.3)	6406.2 (53.7)	6485.3 (85.4)	6787.9 (126.9)
VAE + VAMPRIOR	5842.2 (82.8)	6273.8 (86.3)	6682.6 (16.8)	6984.6 (7.4)
★ VAE + VAMPRIOR	6538.3 (62.4)	6595.9 (93.8)	6852.3 (18.6)	6966.1 (28.0)

Table 9: Evaluation of all methods in terms of test log marginal likelihood (*the higher, the better*) of VAE models on CELEBA. The same interpretation as Table 3.

I.3 More qualitative results

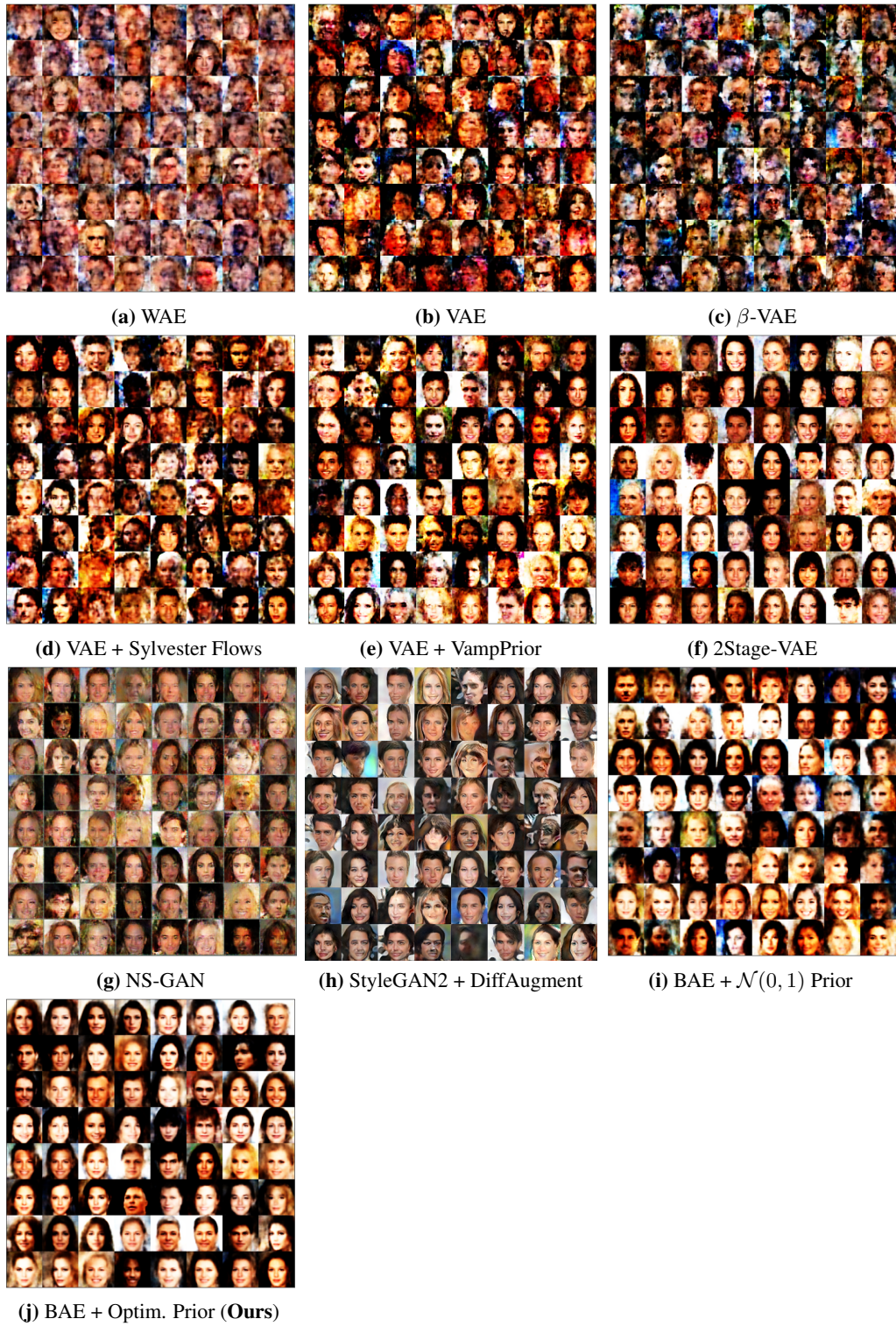


Figure 17: Qualitative evaluation for sample quality for autoencoders and GANs on CELEBA. Here, we use 500 samples for training/inference.

CELEBA - RECONSTRUCTIONS	
GROUND TRUTH	
★ WAE	
★ VAE	
★ β -VAE	
★ VAE + SYLVESTER FLOWS	
★ VAE + VAMPRIOR	
★ 2-STAGE VAE	
★ BAE + $\mathcal{N}(0, 1)$ PRIOR	
BAE + OPTIM. PRIOR (OURS)	

Table 10: Qualitative evaluation for reconstructed samples on CELEBA. ★ indicates that we use the union of the training data and the data used to optimize prior to train the model. Here, the training size is 1000.

MNIST - RECONSTRUCTIONS	
GROUND TRUTH	
WAE	
★ WAE	
VAE	
★ VAE	
β -VAE	
★ β -VAE	
VAE + SYLVESTER FLOWS	
★ VAE + SYLVESTER FLOWS	
VAE + VAMPRIOR	
★ VAE + VAMPRIOR	
2-STAGE VAE	
★ 2-STAGE VAE	
BAE + $\mathcal{N}(0, 1)$ PRIOR	
★ BAE + $\mathcal{N}(0, 1)$ PRIOR	
BAE + OPTIM. PRIOR (OURS)	

Table 11: Qualitative evaluation for reconstructed samples on MNIST. ★ indicates that we use the union of the training data and the data used to optimize prior to train the model. Here, the training size is 200.

MNIST - GENERATED SAMPLES	
WAE	1 3 0 9 2 5 9 2 7 2 3 1 1
★ WAE	4 3 5 6 6 8 0 3 8 5 2 3 5 0
VAE	2 3 9 9 3 4 7 7 7 3 8 3 9 9
★ VAE	7 2 0 4 4 9 0 2 0 0 4 4 3 3
β -VAE	9 3 7 9 2 4 1 4 7 3 6 8 7 4
★ β -VAE	8 2 7 5 2 4 0 3 4 5 3 2 3 2
VAE + SYLVESTER FLOWS	3 3 5 1 8 6 4 9 6 9 5 9 2 1
★ VAE + SYLVESTER FLOWS	5 0 4 4 6 0 6 2 5 0 9 0 2 0
VAE + VAMPRIOR	1 5 5 5 7 7 7 8 6 5 3 5 5 2
★ VAE + VAMPRIOR	8 4 5 2 8 0 9 5 0 8 2 0 6 8
2-STAGE VAE	7 2 6 3 6 4 4 7 4 4 8 4 1
★ 2-STAGE VAE	5 0 4 4 6 0 6 2 5 0 9 0 2 0
BAE + $\mathcal{N}(0, 1)$ PRIOR	3 1 1 1 6 1 2 2 9 9 9 9 9 9
★ BAE + $\mathcal{N}(0, 1)$ PRIOR	3 3 3 1 9 2 5 9 7 7 7 3 3 3
BAE + OPTIM. PRIOR (OURS)	9 3 3 1 0 2 4 9 7 3 5 8 6 6

Table 12: Qualitative evaluation for generated samples on MNIST. ★ indicates that we use the union of the training data and the data used to optimize prior to train the model. Here, the training size is 200.

YALE - RECONSTRUCTIONS	
GROUND TRUTH	
WAE	
★ WAE	
VAE	
★ VAE	
β -VAE	
★ β -VAE	
VAE + SYLVESTER FLOWS	
★ VAE + SYLVESTER FLOWS	
VAE + VAMPRIOR	
★ VAE + VAMPRIOR	
2-STAGE VAE	
★ 2-STAGE VAE	
BAE + $\mathcal{N}(0, 1)$ PRIOR	
★ BAE + $\mathcal{N}(0, 1)$ PRIOR	
BAE + OPTIM. PRIOR (OURS)	

Table 13: Qualitative evaluation for reconstructed samples on YALE. ★ indicates that we use the union of the training data and the data used to optimize prior to train the model. Here, the training size is 500.

YALE - GENERATED SAMPLES	
WAE	
★ WAE	
VAE	
★ VAE	
β -VAE	
★ β-VAE	
VAE + SYLVESTER FLOWS	
★ VAE + SYLVESTER FLOWS	
VAE + VAMPRIOR	
★ VAE + VAMPRIOR	
2-STAGE VAE	
★ 2-STAGE VAE	
BAE + $\mathcal{N}(0, 1)$ PRIOR	
★ BAE + $\mathcal{N}(0, 1)$ PRIOR	
BAE + OPTIM. PRIOR (OURS)	

Table 14: Qualitative evaluation for generated samples on YALE. ★ indicates that we use the union of the training data and the data used to optimize prior to train the model. Here, the training size is 500.